




Article

Relative Abundance and Compositional Variation of Silicates, Oxides and Phosphates in the W-Sn-Rich Lodes of the Panasqueira Mine (Portugal): Implications for the Ore-Forming Process

António Mateus ^{1,2,*} , Jorge Figueiras ^{1,2}, Ivo Martins ², Pedro C. Rodrigues ^{1,2}  and Filipe Pinto ^{3,4} 

¹ Departamento de Geologia, Faculdade de Ciências da Universidade de Lisboa, Ed. C6, Piso 4, Campo Grande, 1749-016 Lisboa, Portugal; jfigueiras@fc.ul.pt (J.F.); pcrodrigues@fc.ul.pt (P.C.R.)

² Instituto Dom Luiz (IDL), Faculdade de Ciências da Universidade de Lisboa, Ed. C1, Piso 0, Campo Grande, 1749-016 Lisboa, Portugal; ijmartins@fc.ul.pt

³ Beral Tin and Wolfram, S.A., Geology Department, 6225-051 Barroca Grande, Portugal; filipe.pinto@beraltportugal.pt

⁴ Instituto de Ciências da Terra (ICT), Pólo da Universidade do Porto, Rua do Campo Alegre 687, 4169-007 Porto, Portugal

* Correspondence: amateus@fc.ul.pt

Received: 17 April 2020; Accepted: 15 June 2020; Published: 19 June 2020



Abstract: Panasqueira is a world-class W-Sn-Cu lode-type deposit located in Portugal. It consists of a dense swarm of subhorizontal quartz lodes criss-crossed by several ENE–WSW and N–S fault zones, bordering Late Variscan granite and hosted in Late Ediacaran—Early Cambrian metasediments. The relative abundance and compositional variation (assessed with EPMA) of the main silicates, oxides and phosphates forming the quartz lodes and their margins were examined, aiming to explore: (i) mineral and geochemical zonation at the mine scale; and (ii) some conclusions on the chemical nature of prevalent fluid inflows and *T*-conditions of mineral deposition. Quartz lodes nearby or far from the known greisen-granite cupola display significant differences, reflecting multiple fluid influxes of somewhat distinct composition related to various opening and closing events extending for several My, ranging from an early “oxide–silicate stage” (OSS) to a “main sulfide stage” (MSS), and further on to a post-ore carbonate stage (POCS); however, a rejuvenation event occurred after MSS. The onset of OSS was placed at ca. 299 ± 5 Ma and the rejuvenation event at ca. 292 Ma. The OSS was confined to $\approx 500 \leq T \leq 320$ °C, following rutile and tourmaline growth under $\approx 640 \leq T \leq 540$ °C (depending on *a*SiO₂). The rejuvenation event (≈ 440 – 450 °C) preceded a late chlorite growth (≈ 250 – 270 °C) and the progression towards POCS.

Keywords: granite-related W-Sn mineralization; NW Iberian Variscides; Panasqueira deposit; mineral composition variations; mineral thermometry

1. Introduction

Granite-related deposits represent a natural source of various ore minerals, incorporating a large suite of metals necessary for an increasing number of industrial and technological applications [1–3]. Threats regarding possible shortages of some raw materials in the future, along with the need to diversify the suppliers, have been instrumental to fostering a renewed interest in deepening the current knowledge on these deposits and the processes involved in their formation. New advances have already been achieved [4–11], but additional work is required to suitably address the highly diversified

mineral assemblages, incorporating valuable by-products and the fingerprints or footprints that should be used in modern exploration surveys oriented to concealed granite-related ore systems.

In Europe, numerous granite-related deposits and occurrences define a well-known Late Paleozoic metallogenic belt, extending from the Bohemian Massif via French Massif Central, Armorica, and Cornwall to NW Iberia [12–22]. These ore systems comprise varied styles of W and Sn mineralization, often coexisting with rare element (e.g., Li, Cs, Ta, Be) pegmatites, which are associated with different voluminous suites of peraluminous granites mostly generated and emplaced during the 320–290 Ma time window [23–34]. Recent reassessments of critical factors determining the development of this belt and its metal endowment [35–46] provided many innovative insights, showing that ore-forming processes are synchronous of the main exhumation stages of the European Variscan cordillera and that conventional genetic models should be reviewed [47–52]. In fact, these ore-forming processes can no longer be interpreted simply as a result of the emplacement of single intrusions that generate large amounts of fluids at the summit of the granite cupola during its fractionated crystallization, and also promote the growth of divergent fracture sets above the cupola, depending on the confining pressure. On the contrary, the location, size and metal enrichment of mineralized systems relative to granite emplacement should depend on many geodynamic, chemical and structural key parameters acting in different time and spatial scales, and ruling: (i) the distribution of fertile protoliths involved in the generation of granite melts; (ii) the conditions under which crustal melting took place, influencing the redistribution of ore-forming and fluxing elements as melt forms; (iii) the long-lived magmatic and thermal history of large metal-rich deposits; and (iv) the most critical pathways and timeframes for fluid flow and interactions with country rocks, thus controlling the mineralization style and composition, as well as its vertical and lateral extension.

The Panasqueira W-Sn-Cu deposit, located in Portugal, is a paradigmatic case of the Late Palaeozoic, granite-related European metallogenic belt. It is the main known tungsten deposit in Europe (the 9th largest worldwide) and has operated almost continuously since 1896. The historical records indicate over 110,000 tons of wolframite concentrate produced since 1947, along with several thousand tons of cassiterite and chalcopyrite concentrates [53]; significant amounts of zinc, lead and silver-rich mineral concentrates were also produced throughout the time when the old Rio sulfide treatment plant was fully operational. During the protracted exploitation history of the Panasqueira mine, many geological, mineralogical and geochemical studies have been conducted [54–62]. However, several questions still remain open, and some interpretations highlighted in previous analyses are arguable in light of new findings, which prove the uniqueness of the deposit and its remarkable heterogeneity. The search for answers that might help resolve these questions is vital for the understanding of causes controlling the development of first class, granite-related, W-Sn lode-type deposits in NW Iberia Variscides and other comparable geological settings. The present work intends to address some key issues related to the chemical nature of prevalent fluid inflows and temperature conditions of mineral deposition, as recorded by the compositional variation of the main silicates, oxides and phosphates forming the quartz lodes of the Panasqueira mine. To this end, a large mineral database will be reported and discussed, documenting a systematic survey of 215 samples representing all the accessible mine sectors and underground mining levels. The obtained results contribute to an exploratory mapping of particular mineralogical and geochemical features, which may help assess possible compositional zonings at the deposit scale, providing clues about the superposition of ore-forming processes possibly controlled by distinct sources and structures.

2. Geological Background

The Panasqueira world-class deposit, as with many other W and Sn ore systems in NW Iberia, is located in the Central Iberian Zone (Figure 1). In this major geotectonic unit of the autochthon Variscides, various suites of voluminous granite intrude thick sedimentary successions of prevailing siliciclastic nature. These sediments, grouped into several geological formations of different ages, are affected by low-grade metamorphic recrystallization (usually under greenschist facies conditions)

and by poly-phasic Variscan deformation, from D1 (359–336 Ma) to D3 (315–306 Ma) ([63,64] and references therein). The most significant sedimentary pile corresponds to a flysch-like succession of Late Ediacaran to Early Cambrian age unconformably overlain by an Ordovician quartzite-dominated succession. In Portugal, the flysch-like succession is usually divided into the Douro and Beira Groups, the latter including the country rocks of Panasqueira lodes. The main group of granite shows peraluminous affinity [65–75] and represents melts generated during an extensive event of crustal anatexis (325–311 Ma; [76–78]) which were emplaced episodically during D3. However, additional melts were produced and settled after D3 [79–84]. Therefore, considering the available geochemical and isotopic dataset for all the studied granite bodies, it is convenient to distinguish the suites emplaced at ca. 320–315 Ma, 310–305 Ma, and 296–290 Ma, mainly because they are also associated with different types or styles of mineralization [85–100]. Moreover, these three time periods are coeval with the progression of some other geological processes with relevance to the orogenic belt structure and related metallogeny, ruling the nucleation or propagation and subsequent reactivation of large-scale shear zones, and subsequently of a widespread network of strike-slip fault zones [101–105]. Both structural sets display discontinuous and multistage (often mineralized) hydrothermal mineral infillings, documenting their role in the long-lasting control of crustal permeability and focused fluid flow [106,107]. As a result, at a local scale and in the presence of suitable structural arrays, many primary features of early-formed mineralization could be significantly affected by late imprints related to the circulation of fluids with distinct compositions. These imprints could even lead to the generation of quite different mineralization types, spatially coexisting with previous lodes but often presenting a distinct structural control [107–112].

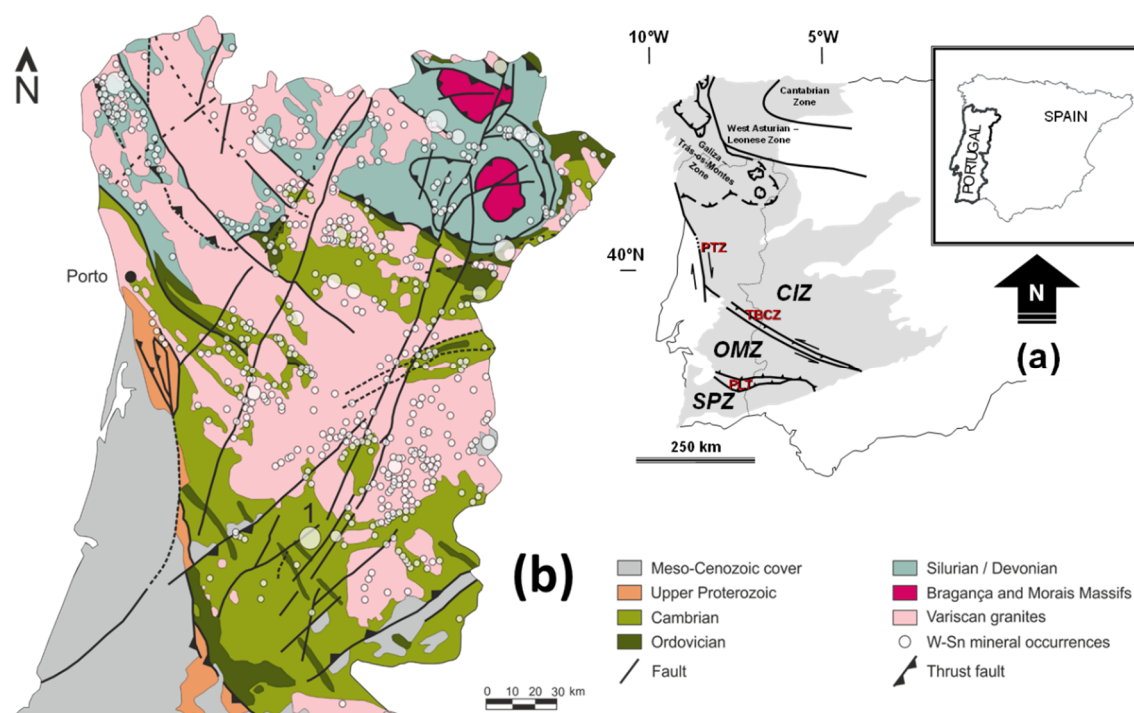


Figure 1. (a) Schematic illustration of the main geotectonic units in the Iberian Variscides and some major shear zones: CIZ—Central Iberian Zone; OMZ—Ossa–Morena Zone; SPZ—South Portuguese Zone; PLT—Pulo do Lobo Terrane (contiguous to the SW Iberian suture); PTZ—Porto–Tomar Shear Zone; TBCSZ—Tomar–Badajoz–Córdoba Shear Zone. (b) Simplified geological map of central and northern Portugal with locations of the main tungsten and tin deposits identified to date. 1—Panasqueira Mine. Adapted from “Carta Geológica de Portugal 1:1,000,000”, Geological Survey of Portugal, LNEG, 2010. Information on mineral deposits provided by the official national catalogue SIORMINP (LNEG).

The Panasqueira Deposit

The Panasqueira deposit consists of a dense swarm of quartz lodes criss-crossed by several ENE–WSW and N–S fault zones, bordering Late Variscan granite and hosted in a tightly folded metasedimentary succession belonging to the Beira group (Figure 2a). All over the eastern sector of the mine concession, metasediments include fine-grained andalusite blasts, whose spatial distribution outline a NW–SE elongated contact metamorphic rim related to a concealed granite body that bears no simple relationship to a greisenized cupola intersected in underground works. This complexity opens the possibility of a huge batholith being present at depth, throwing out multiple large-sized apophyses, or else the possibility of several hidden granite cupolas. Both alternatives are plausible considering the available (still limited) geochronological, geochemical and geophysical data, even though the latter hypothesis has been favored in several studies [113–115].

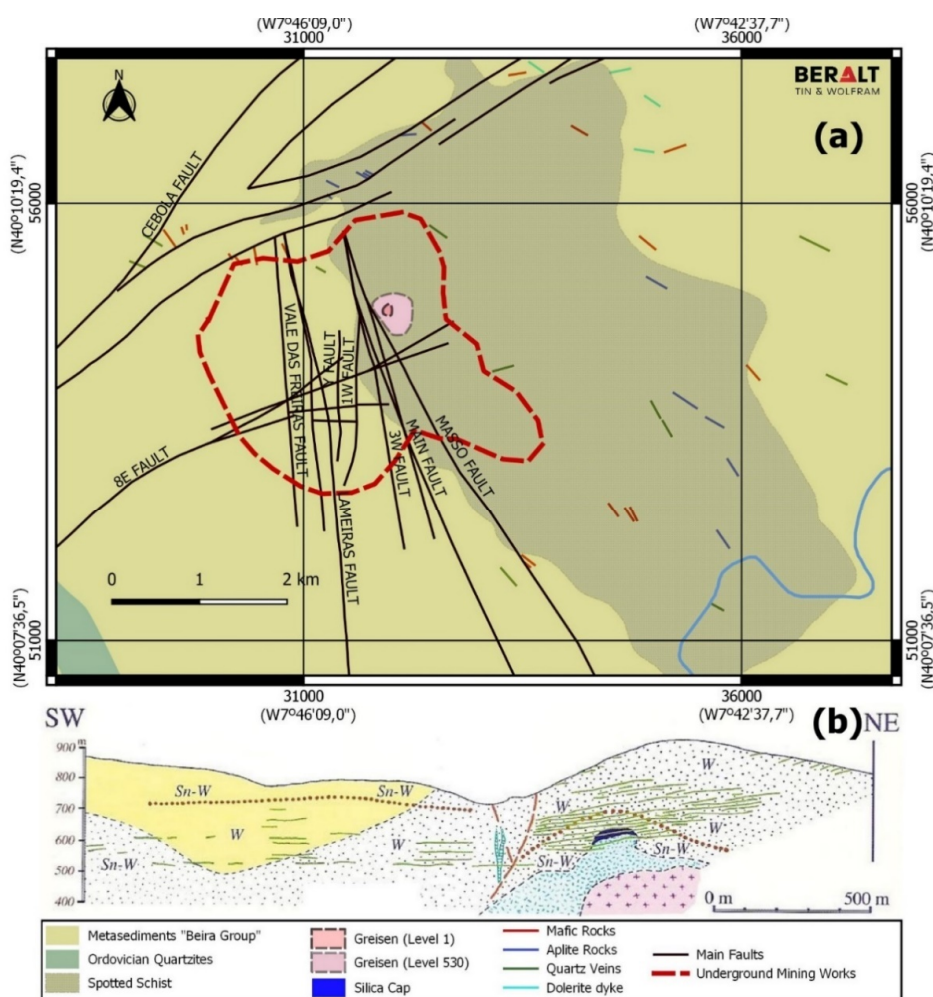


Figure 2. Geological map of the Panasqueira mine area (a) and geological cross-section of the Barroca Grande sector (b), across the swarm of quartz lodes bordering the greisen-granite cupola (dotted pattern fill with a light-blue foreground); in this cross-section, the spotted schists are indicated by the dotted pattern filled with the black foreground and separated from the other metasediments (in yellow). Adapted from the official map of Beralt Tin and Wolfram Portugal, after [56,57,69].

The mined quartz (\pm topaz \pm white mica \pm tourmaline \pm siderite) lodes are irregularly distributed in a global volume that extends for ca. 2500 m in length, ca. 400 to 2200 m in width, and ca. 500 m in depth (Figure 2B). Prevalent lodes are subhorizontal (8° to 10° SW) and display an average thickness of 0.30 m, ranging from 0.05 to 1.0 m; these structures are complemented by several subsets of subvertical quartz

veins, which are usually thinner and less enriched in mineral ore phases [57,109,116–121]. Some segments of the ENE–WSW and N–S fault-zones also comprise mineralized hydrothermal infillings [122–125]. In general, high-grade lodes comprise variable amounts of wolframite or cassiterite, sulfides (typically chalcopyrite, arsenopyrite, sphalerite, pyrrhotite, pyrite, stannite, galena, and Bi–Ag-bearing phases) and Bi alloys [57,58,62,126]. Alongside these lodes, alteration haloes affecting the hosting metasediments are usually observed, extending up to 2 m away from the thicker lodes and characterized by intense deposition of tourmaline, along with accessory white mica \pm chlorite [59,127,128].

Many studies have been carried out in the Panasqueira deposit since 1943 and a remarkable body of knowledge on a large number of issues has been generated. Nonetheless, several crucial features implicated in the ore-forming process and lode growth are still controversial or remain poorly understood. Significant advances were indeed achieved regarding key conditions for the development of the quartz lodes and their possible relation to the known greisen-granite cupola [57–62,129,130]. However, different interpretations persist of the prevailing fluid pathways, and consequently of the parameters used in physical flow modelling [131–133]. Previous works also established that the ore-forming process should have progressed from an early “oxide–silicate stage” (OSS) to a “main sulfide stage” (MSS), and further into a post-ore carbonate stage [57,61]. However, this general evolving scenario hardly considers details about the distribution of many accessory phases and possible geochemical zonings at the mine scale, which might rule the predominance of specific mineral assemblages or particular variations in mineral compositions [126,134–137]. Various improvements were also made in the search for the time window during which the ore-forming processes took place [138–140], notwithstanding the difficulties of collecting a representative geochronological dataset for the main evolving stages of the ore system. The composition and origin of the mineralizing fluids were likewise addressed in many studies, making use of complementary approaches [58,113,128,130,141–151]. Even so, doubts subsist on the nature of the fluid sources involved in some stages of ore formation, as well as on their P–T–X–t paths. Furthermore, some ideas concerning metal enrichment mechanisms were explored in a few surveys [113,115,123,152], not necessarily favoring simple magmatic–hydrothermal affiliations with the known greisen-granite cupola. However, these are not free of controversy and much work is still needed to trace the metal sources and understand the processes implicated in the generation of high-grade lodes in this unique deposit.

3. Sampling and Electron Probe Microanalyzer Analytical Conditions

Underground works at the Panasqueira mine spread for ca. 2.2 km from the greisen-granite cupola to the WSW and SSW, along four horizontal levels connected by ramps and spaced 60 m (L0 to L2) and 90 m (L2 to L3) apart. A comprehensive sampling program covering all the accessible sectors of the mine and its exploitation levels was carried out during 2016. The resulting 197 samples (Figure 3) were added to another 18 samples collected in March 2015 at the underground level L1 and 15 more samples picked from various outcrops within the mine concession. Of these 230 samples, 210 polished thin sections were produced and examined with conventional optical microscopy.

A systematic characterization of the mineral composition variation was made with a JEOL-JXA 8200 electron probe microanalyzer (EPMA) equipped with four wavelength-dispersive spectrometers (WDS) and one energy-dispersive X-ray spectrometer (EDS). An optimization of the EPMA analytical conditions needed to detect and measure a large number of chemical elements that might be incorporated in silicates, oxides and phosphates was previously performed, setting the analytical profile to be used in each mineral group. The quantitative analyses were conducted with an accelerating voltage of 15 kV and a beam current of 25 nA. The beam diameter was set at 5 μ m and each element was counted for 20 s on the peak and 10 s on the background. Table S1 (Supplementary Materials) summarizes the information on the standards used in each analytical profile and the average detection limits for the intended elements. Elemental concentrations were determined using the ZAF software provided by JEOL. For each analysis, the detection limits for each analyzed element were estimated with JEOL software using background statistics and the 3-sigma criterion:

$$CDL = 3 \times [(2N_b/T_b A_{samp})0.5/((N_{std}/C_{std}) \times (i_{samp}/i_{std}))] \times 10,000 \quad (1)$$

where N_b is the average intensity of the background (cps/ μ A) measured on the sample, T_b is the total counting time of the background (s) for the sample, A_{samp} is the number of accumulation on the sample, N_{std} is the net intensity of the standard (cps/ μ A), C_{std} is the concentration of the standard (wt %), and i_{samp} and i_{std} are the probe currents measured for the standard and sample (μ A), respectively. The tabulated detection limits were set at the 95th percentile of the individual estimations for each homogeneous group of analyses; that is, for analyses of the same mineral or of minerals with similar chemical composition. The evaluation of the major element distribution in crystals (zoning) and crystal groups (variability) in every zone of interest required the collection of significant numbers of analyses—typically 10 or more per zone or mineral. The minor element concentration in each crystal or zone was then evaluated with improved statistics by either accumulating these analyses, with degradation of spatial resolution, or by validating their statistical significance based on the fraction above the detection limit. A similar approach was used to validate homogeneous groups of elements, because even if the measurement of each individual element has insufficient statistics to be considered above the detection limit, their combined measurements may have robust enough statistics to make it evident that the group as a whole is being detected. This is especially the case for the rare earth elements (REE), but may apply to any group of low-concentration elements, which as an example may share a common structural site in a mineral. The standard analytical relative errors (2σ) involved in the measurements were 2% for all the elements in each mineral phase.

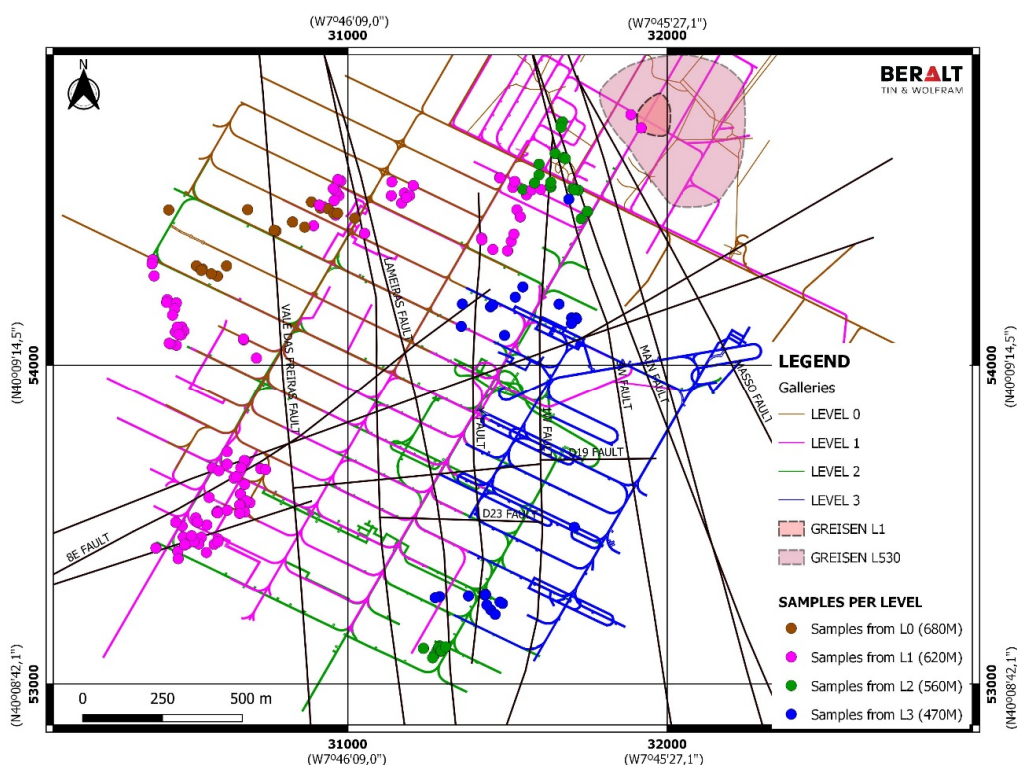


Figure 3. Sampling program in underground mining works carried out for the present study at the Barroca Grande sector placed to the south of Panasqueira and Vale Ermida sectors (indicated in the map by some old galleries). Heights L0, L1, L2, and L3 are altitudes in relation to the sea level.

The calculation of empirical formulas was performed in the usual manner whenever possible. The normalization factors were calculated on the basis of the total number of atoms or of the total charge revealed by each individual analysis. This straightforward procedure does not yield accurate results if the quantity to be used as a normalization basis does not have a measured experimental value, which is very often the case when an EPMA is used due to its inability to efficiently analyze elements with $Z < 9$.

This results in inaccurate stoichiometric coefficients in the calculated empirical formulas and precludes any reliable estimation of the concentrations of the non-analyzed elements. It has been shown in the past [153,154] that for very special cases, algebraic procedures can be devised to correctly normalize incomplete analyses, whether by resorting to alternative but seldom used normalization bases, or by simultaneously using two different normalization bases. In the present work, a specially designed algebraic method (manuscript in preparation) was used, seeking out the value of the normalization factor that simultaneously satisfies every possible normalization basis revealed by the ideal formula of the mineral, together with any additional stoichiometric constraint that can be shown to hold in the mineral under consideration. The algebraic procedure is of universal application, but the normalization bases and other stoichiometric constraints are specific for each mineral group. For tourmaline, the total number of atoms, excluding those in the *A*-site (assuming $B = 3$), and the total charge (again assuming $(OH)^X = 3$ and $(OH + F + Cl)^Z = 1$) were used; additionally, a stoichiometric invariant involving *D* and *G* trivalent cations, *A* cations and Li—which was verified in an exact form in all of the non-oxide tourmaline ideal endmembers and so was deemed to hold for every combination of these endmembers—were also considered. For micas, because of the lack of evidence for strong oxidation, $(OH + F + Cl) = 2$ was assumed, while the sought-out normalization factor simultaneously satisfied both the total charge and the complex relationship between octahedral charge, tetrahedral charge and the *A*-site' occupation and charge, which holds for all mica endmembers; once again, this was deemed to hold for every combination of these endmembers. If successful, the procedure calculates an adequate normalization factor and reconstitutes the correct empirical formula, giving the stoichiometric coefficients of both the analyzed elements and of the non-analyzed ones (also including the Fe^{2+} – Fe^{3+} partitioning in these). Failure to do so or to yield an analytical summation close to 100 wt % after inclusion of the non-analyzed elements leads to rejection of the analyses. Analyses of each mineral group were split into different subgroups according to petrographic information. This procedure gave evidence of variations in compositions recorded in distinct generations of the same mineral phase. Additional efforts were done to investigate possible relations between compositional changes and sampling sectors. Each subgroup of analyses was also examined to obtain the representative compositional data, i.e., the statistically meaningful concentration values for major and minor elements, complemented by the significant trace elements whenever valid.

4. Distribution of Silicates, Oxides and Phosphates in Lodes and Their Margins, and in Greisen

The Panasqueira lodes comprise a diverse mineral array that is not evenly recorded in all of the mine sectors. Additionally, many phases occur in specific settings of the lodes, documenting particular steps of their development. Thus, a complete range of observation scales, covering the largest possible number of lodes occurring in different parts of the deposit, is critical to support the correct interpretation of mineral and textural arrangements preserved in the lode system. The systematic inspection of underground mining exposures and hand specimens shows that apart from quartz, the most common silicates are tourmaline, white mica and topaz. At these scales, the prevalent oxide minerals are wolframite and cassiterite, and the usual phosphate is apatite. Microscopic observations reveal that chlorite must be added to the typical silicate assemblage of Panasqueira lodes, rimming white mica or sulfide aggregates, or sealing late fractures with variable geometry and orientation. Rutile, which regularly accompanies tourmaline in many lode walls, is another relevant oxide phase, however this demands a thorough petrographic examination for definitive identification. The same is true for many phosphates other than apatite, whose complete characterization requires supplementary means of analysis, such as EPMA.

4.1. Tourmaline

Alteration haloes adjoining the quartz lodes of Panasqueira are most often enriched in tourmaline and criss-crossed by quartz–sulfide veinlets, therefore indicating a relatively early deposition timing for this B-silicate. Locally, whenever a dense fracture network affects the hosting metasediments

(usually reflecting superimposed, multiphase brittle deformation), the alteration haloes become quite evident and coarse-grained tourmaline aggregates develop (Figure 4a). This tourmaline (*Tour Ia*) is often deposited along with white mica \pm apatite (*Apt I*) \pm rutile \pm quartz and at the microscale the grains display frequently irregular borders and strong optical zonation (pale- to deep-green cores and brownish to brown rims); regularly, the cores of these crystals are characterized by patchy zoning (Figure 4b,c). When the alteration haloes are not so clear, *Tour Ia* is confined to the lode borders or decorates the edges of metasediment slivers incorporated in the lodes (Figure 4d); occasionally, minute cracks sealed with tourmaline, quartz, rutile, and monazite are observed. In these settings, *Tour Ia* forms fine- to medium-grained prismatic crystals and also shows evident optical zonation, similar to that seen in the coarse-grained aggregates, although presenting fine-scale oscillatory zoning; the cores of the larger crystals frequently include tiny inclusions of apatite and quartz (+ rare monazite) that are only resolved with very high magnifications.

The timing of lode margin *Tour Ia* growth should not deviate significantly from that associated with the main stage of white mica (*Ms Ia*) deposition (see below) but should precede the development of *Tour Ib* and *Tour Ic* occurring, respectively, as tiny euhedral crystals in thin selvages of white mica and topaz (*Ms Ib* and *Tpz Ib*, see below) and as infillings of microfractures that cross over previously deposited mineral arrangements (Figure 4e–g). The optical zonation of *Tour Ib* and *Tour Ic* is delicate, ranging from pale- and deep-green cores to brownish rims.

The growth of *Tour Ib* and *Ic*, although differing in time, took place during the early “oxide–silicate stage” (OSS), clearly preceding the period when large (often massive) sulfide aggregates formed. Therefore, *Tour Ib* and *Ic* occurrences are distinct from those typifying *Tour II*, which are characterized by acicular or radial clusters of very thin prisms that display subtle concentric optical zonation (pale-greenish cores and almost colorless rims). *Tour II* clusters (Figure 4h), frequently associated with non-deformed quartz (*Qz II*) but preceding euhedral apatite (*Apt II*), along with white mica rosettes (*Ms II*) and late carbonates, occur as infillings of interstitial spaces (sometimes resembling small pockets) generated during fracturing events that affect many lodes. Since these fracture arrays disrupt mineral assemblages representing the OSS and the “main sulfide stage” (MSS), their infillings should cause a distinct fluid influx into the lode system.

4.2. White Mica

White mica is an accessory phase in alteration haloes around quartz lodes, where it occurs as fine-grained (<1 mm) flakes coexisting with *Tour Ia* (\pm apatite \pm rutile \pm quartz). However, at the walls of many lodes, white mica growth can be conspicuous (*Ms Ia*), usually developing coarse-grained plates in dense-bladed or feather-like arrangements subperpendicular to the lodes’ walls and rooted in them. Two different subgroups of *Ms Ia* can be distinguished. The first one, preceding the deposition of wolframite (*Wolf I*), includes very large mica plates in thick (up to several centimeters), continuous selvages also enriched in *Tour Ia* (mostly in the E–NE sectors of the mine, Figure 4i,j) or coarse-grained micas in lode walls variably enriched in topaz (*Tpz Ia*) and cassiterite (common in the W–NW sectors of the mine, Figure 4k). The second subgroup of *Ms Ia* comprises oriented coarse-grained micas in thinner selvages with accessory amounts of tourmaline or topaz, occasionally affected by (minor) events of microfracturing prior to the main development stages of the lodes (Figure 4l). The microfractures related to these events are of limited extension and are poorly represented in many sectors of the mine, but their sulfide-rich infillings (*Ia*) show that deposition of some chalcopyrite + arsenopyrite \pm pyrite \pm sphalerite occurred episodically before *Wolf I*. These sulfides, and some discrete disseminations of arsenopyrite (\pm sphalerite) within *Ms Ia* selvages, are not volumetrically important, but their presence at the onset of OSS shows intermittent incursions into the system of fluids with variable compositions.

Fine-grained and non-oriented white mica aggregates (*Ms Ib*) also cover many lode walls, usually developing narrow (<2 cm) and quite often discontinuous bands that also include accessory amounts of *Tour Ib* and topaz (*Tpz Ib*). These types of lode borders are common in, but not exclusive of, the SE mine sectors (Figure 5a,c,d). Their growth is interpreted as coeval of mica infillings along fractures

affecting the OSS mineral assemblages, including the *Ms Ia* thick selvages (Figure 5f), locally connected with microfractures criss-crossing large arrays of *Wolf I* crystals (Figure 5e). In some samples, thin (<1 mm) caps of *Ms Ib* enclose fine-grained sulfides (*Ib*) deposited after *Wolf I*, which are not ascribed to MSS since they are embedded in early quartz aggregates (*Qz Ia*), which display optical effects and microstructural features denoting significant intracrystalline deformation.

White micas formed during the late phases of OSS (*Ms Ic*) seal intergranular spaces of *Qz Ia* aggregates or occur as fracture infillings affecting the mineral assemblages that typify this evolving stage (Figure 5g,h). These micas are distinct from those developing millimeter-sized rosettes or globular masses of dense flakes (*Ms II*-Figure 5i,j), which are common in lodes comprising abundant *Apt II* beside a second generation of topaz, wolframite and cassiterite (see below). Finally, a very late mica (*Ms III*) was observed in various samples as fine-grained (occasionally botryoidal) aggregates that seal small cavities or fractures crossing over the main carbonate masses (and minor sulfides) typical of the post-ore evolving stage.

4.3. Topaz

Lodes bordered by thick topaz selvages (*Topz Ia*) variably enriched in cassiterite and comprising accessory amounts of rutile are common in the SW sector of the mine (Figure 5k) and transition towards the NW sector (Figure 6a–c). These selvages include one or several centimeter-sized bands of light-green massive topaz aggregates showing intense fracturing and heterogeneous sericitization; no mica selvage forms in these lodes. However, in the NE sectors of the mine, some amounts of *Topz Ia* occur in coarse-grained *Ms Ia* selvages that also comprise cassiterite (Figure 6d). The narrow bands of *Ms Ib* decorating some other lode walls (most common in the SE sectors of the mine) also include topaz (*Topz Ib*), which is slightly less colored and fractured in comparison with *Topz Ia* (Figure 6e). A late generation of topaz (*Topz II*), often developing incipiently fractured subhedral grains (Figure 6f), can be distinguished in lodes comprising abundant *Ms II*, *Apt II* and other phosphates (see below). This mineral association is observed in many quartz lodes, particularly in the E–NE and NW sectors of the mine.

4.4. Chlorite

Chlorite is a relatively common silicate in the Panasqueira lodes, although it is usually hard to recognize during simple observation of underground mining exposures and hand specimens. This phyllosilicate develops three distinct generations that trace: (i) the fading of OSS along with *Qz Ib* (displaying wavy extinction of variable intensity, being less deformed than *Qz Ia*); (ii) the transition to the carbonate post-ore evolving stage; and (iii) the late hydrothermal activity related to fault zone infillings. The first generation (*Chl I*) includes fine-grained aggregates encircling *Ms Ic* or filling fractures (and small openings related to fracture intersections) affecting *Wolf I* and the accessory sulfides deposited during the OSS (Figure 6g). The fine-grained masses of *Chl II*, which are quite abundant in some samples representing lodes from the E–NE sectors of the mine, enclose sulfide-rich aggregates of variable grain size coexisting with *Ms II*, *Topz II* and *Apt II*; these masses may locally include minor amounts of siderite, but in general they are bordered by large (and zoned) siderite grains. In fault-zones, coarse-grained chlorite (*Chl III*) crystallized along with carbonates and late-deposited sulfides (pyrite, sphalerite and galena), often cementing brecciated quartz infillings.

4.5. Rutile

Disseminated micrometric (10–100 μm) rutile grains are common in the *Tour Ia*-rich alteration haloes. Coarser grains (up to 450 μm) of rutile occur within early-developed cracks adjoining some lode walls, along with *Tour Ia*, quartz and monazite (Figure 6h). In these settings, and whenever observed with high enough magnification (usually requiring EPMA backscattered electron imaging), the cores of rutile grains are often patchy and rimmed by delicate bands, with some of them showing oscillatory zoning (Figure 6i). Occasional minute inclusions of quartz and wolframite were found in the cores and fringes, respectively, of coarser rutile grains. Within thick *Topz Ia* selvages, tiny (<50 μm) and fairly homogeneous rutile grains also occur.

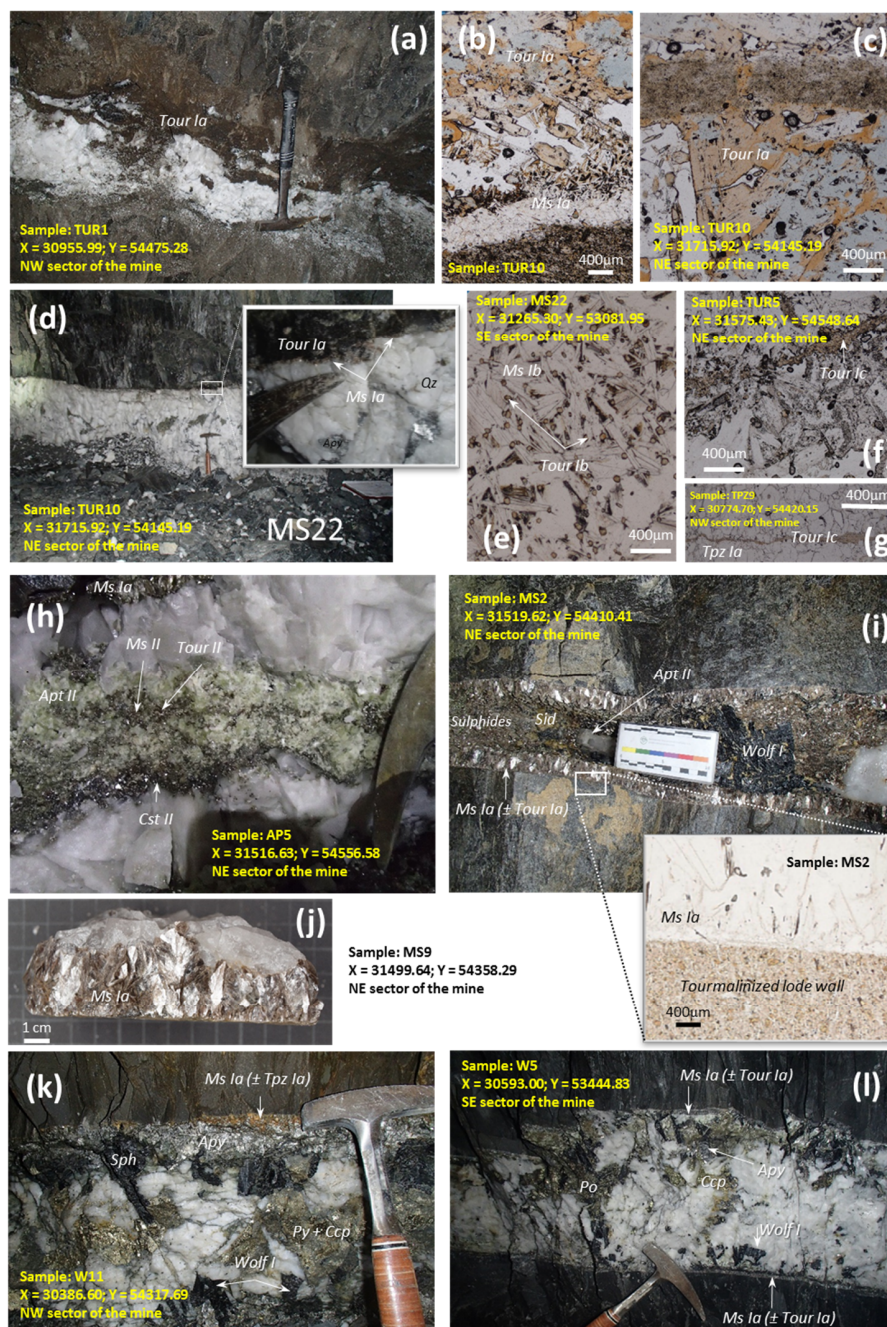


Figure 4. (a) Photograph of the quartz lode wherein the sample TUR1 was collected, illustrating a situation of strong tourmalinization of wall rocks and incorporation of metasediment slivers that are also enriched in *Tour Ia*. (b,c) Photomicrographs (transmitted microscopy, plane-polarized light–TM/PPL) of a tourmalinized wall contacting a lode border decorated by coarse-grained *Tour Ia* (adjoining a *Ms Ia* thin selvage); note the late development a “dissolution band” affecting *Tour Ia*. (d) Photograph of the quartz lode wherein the TUR10 sample was collected. (e) Photomicrograph (TM/PPL) documenting a fine-grained and non-oriented *Ms Ib* aggregate wherein *Tour Ib* is disseminated. (f,g) *Tour Ic* infillings of microfractures crossing over *Ms Ia* (\pm *Qz*) and *TPz Ia* aggregates at the lode borders, respectively. (h) Photograph of the quartz lode wherein the AP5 sample was collected, illustrating a late reopening of the lode that allowed a confined deposition of *Tour II* (as needles), *Apt II*, *Ms II* and *Cst II*. (i,j) *Ms Ia* thick borders of quartz lodes, often contacting tourmalinized walls. (k) Photograph of the quartz lode wherein the W11 sample was collected; coarse-grained *Ms Ia* (\pm *TPz Ia*) in lode walls. (l) Photograph of the quartz lode wherein the W5 sample was collected; coarse-grained *Ms Ia* in thinner selvages along with accessory *Tour Ia*.

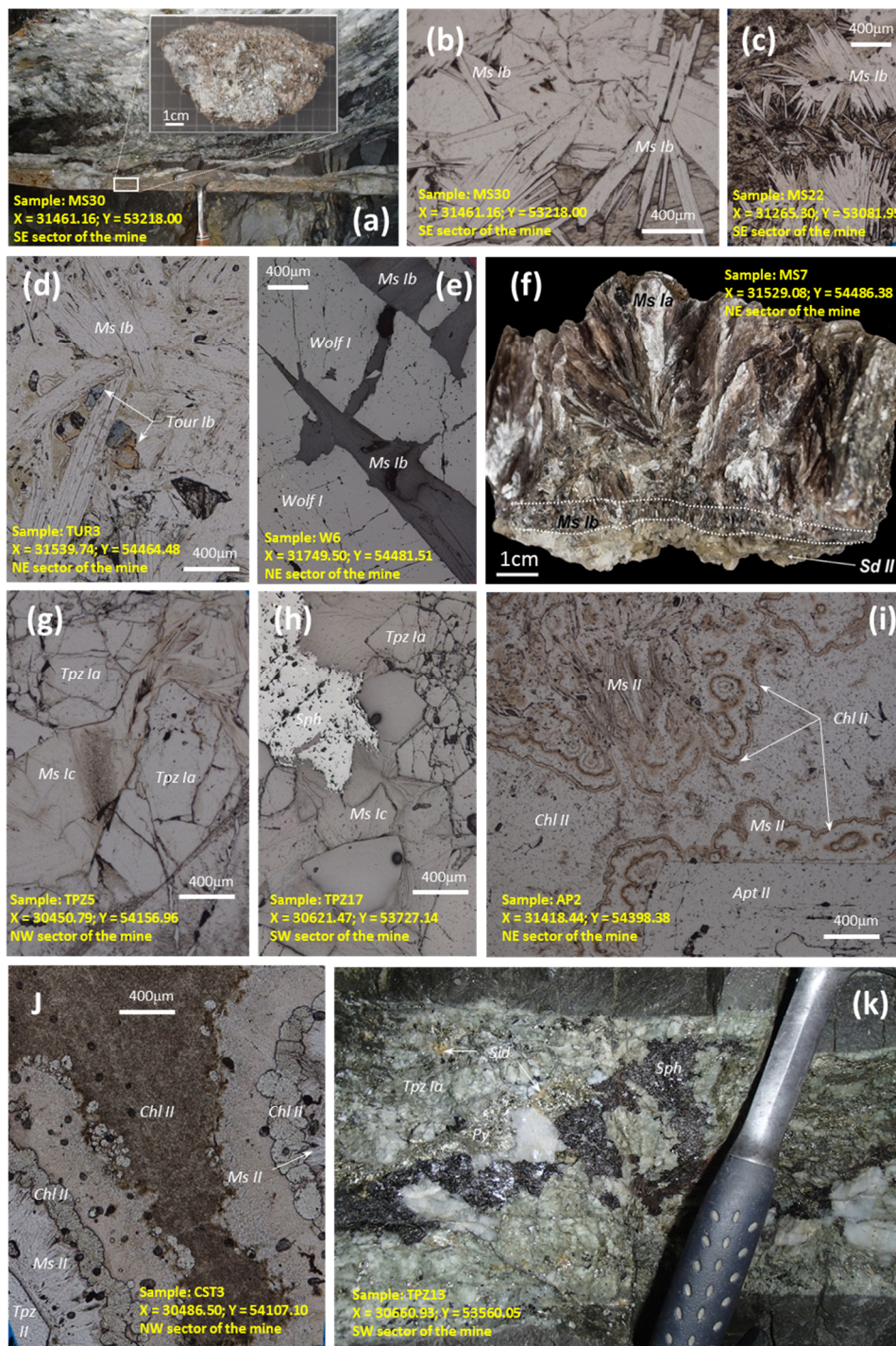


Figure 5. (a) Photograph of the quartz lode wherein the MS30 sample was collected, illustrating the features commonly observed in non-oriented bands of *Ms Ib* at the lode borders. (b–e) Photomicrographs (TM/PPL) documenting different arrangements of *Ms Ib* aggregates, sometimes coming along with accessory *Tour Ib* or forming fracture infillings affecting *Wolf I*. (f) Photograph of a hand specimen showing multiple reopening events at the lode wall, firstly decorated by a thick *Ms Ia* selvage criss-crossed at low angles by a veinlet of *Ms Ib*, later followed by deposition of (subhedral)-euhedral siderite (*Sid II*). (g,h) Photomicrographs (TM/PPL) exemplifying *Ms Ic* growth in intergranular spaces of *Tpz Ia* and *Qz Ia* (+ sphalerite (*Sph*)) + *Tpz Ia* aggregates. (i,j) Photomicrographs (TM/PPL) documenting the typical arrangements of *Ms II*, bordered by *Chl II*. (k) Photograph of the lode wherein the TPZ13 sample was picked, providing evidence for an irregular reopening of a thick *Tpz Ia* selvage (including fine-grained *Cst I*), followed by the deposition of quartz, sulfides (mostly pyrite (*Py*)) and sphalerite (*Sph*) and accessory amounts of siderite (*Sid*).

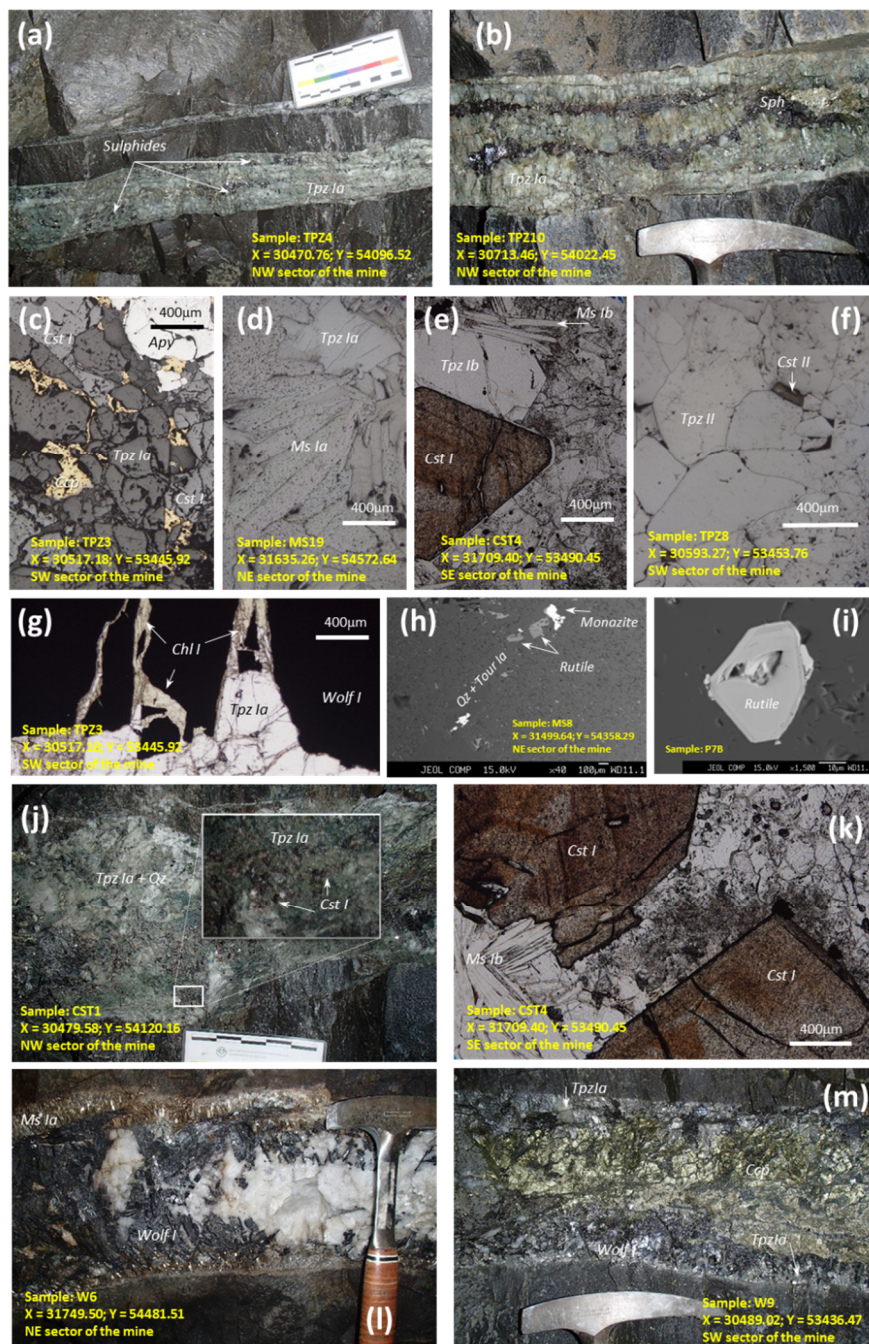


Figure 6. (a,b) Photographs of lodes bordered by thick *Tpz Ia* selvages in the NW sector of the mine, transitional to the SW sector. (c) Photomicrograph (reflected microscopy, plane-polarized light) showing the typical fractured arrangement of (variably altered) *Tpz Ia* and *Cst Ia* aggregates, subsequently irregularly “invaded” by sulfides (arsenopyrite (*Apy*) and chalcopyrite (*Ccp*), in this case). Photomicrographs (TM/PPL) illustrating the growth of: (d) *Tpz Ia* in coarse-grained *Ms Ia* selvages of a lode at the NE sectors of the mine; (e) *Tpz Ib* (and *Cst I*) in narrow bands of *Ms Ib* (+ *Qz*) decorating the walls of a lode at the SE sector of the mine; and (f) *Tpz II* (and *Cst II*). (g) Photomicrograph (TM/PPL) illustrating *Chl I* fracture infillings affecting *Tpz Ia* and *Wolf I*. Back-scattered electron images documenting: (h) rutile in early-developed cracks adjoining the lode wall, along with *Tour Ia*, *Qz* and monazite; and (i) zoned rutile grains included in a *Tour Ia*-rich alteration halo. (j) Photograph of the lode wherein the sample CST1 was picked, exemplifying coarse-grained *Cst I* within *Tpz Ia* thick selvages. (k) Photomicrograph (TM/PPL) representing the typically observed *Cst I* optical zonation. (l,m) Photographs of *Wolf I*-rich lodes bordered by thick *Ms Ia* and *Tpz Ia* selvages, respectively, where the samples W6 and W9 were collected.

4.6. Cassiterite

Coarse-grained euhedral crystals of cassiterite (*Cst I*), often forming centimeter-sized aggregates, occur within *Tpz Ia* thick selvages in quartz lodes distributed across the SW sector of the mine and transition towards the NW sector (Figure 6j). Similar occurrences of *Cst I*, but generally of somewhat smaller grain size, characterize the (*Ms Ia* + *Tpz Ia*)-bearing selvages of lodes in the W–NW sectors of the mine. When topaz is absent or represents no more than an accessory phase of the mineral assemblage outlining the lode walls, *Cst I* grains are quite small and occur as erratic disseminations within white mica masses, largely near the contact areas with wall rocks. In all these settings of the OSS, *Cst I* shows optical (frequently oscillatory) zonation (Figure 6k) and its deposition precedes *Wolf I*. In many samples, *Cst I* coexists with discrete disseminations of arsenopyrite, which are tentatively correlated with sulfide *Ia* deposition.

Two additional late mineral assemblages include cassiterite, both developing after the main sulfide depositional stage (MSS). One of them involves tiny subhedral to anhedral grains of optically homogenous cassiterite (*Cst II*) associated with *Tpz II* and *Ms II* (Figure 6f). The other one, carefully described in recent works [125,126], consists of coarse-grained cassiterite (*Cst III*) merging together with siderite aggregates and speckled with tiny euhedral crystals of pyrite, forming the infilling of a NE–SW subvertical fault zone ($X = 30,484.20/Y = 53,459.90/Z = 628.0$ in Figure 3).

4.7. Wolframite

Wolframite postdates cassiterite and is the main oxide mineral formed during the OSS. In high-grade lodes, this oxide (*Wolf I*) develops variable textural arrangements, mostly from massive coarse-grained aggregates to fan-shaped arrays of (sub)euhedral crystals (Figure 6l). These lodes usually display *Ms Ia* selvages, although there are numerous cases where the lode walls are simply decorated with discontinuous bands of *Ms Ib*. In the former structures, the initial steps of *Wolf I* growth should not deviate significantly from the deposition timing of *Ms Ia* (and lode margin *Tour Ia*), but textural relationships strongly suggest that the main period of mica development is prior to *Wolf I* deposition. Often, *Wolf I* aggregates are distinctly fractured and invaded by *Ib* sulfide phases (chalcopyrite, arsenopyrite and pyrite), with the latter criss-crossed by *Ms Ib* veinlets; also note that the roots of some fan-shaped arrays of *Wolf I* are intersected by *Tour Ic* veinlets. In the lodes bordered by narrow *Ms Ib* bands, *Wolf I* aggregates are often disrupted by various sets of microfractures sealed with this mica and running subparallel to the lode walls; sulfides *Ib* are less important in this setting.

Wolframite is also present in lodes rimmed by thick *Tpz Ia* selvages (Figure 6m), but never reaching the abundance documented for lodes regularly distributed across the E–NE and SE sectors of the mine. Accessory amounts of late wolframite (*Wolf II*) euhedral crystals (usually smaller than *Wolf I* and not developing large masses) can also be found in mineral assemblages developed after the MSS. In these settings, *Wolf II* is typically enclosed by *Ms II* or aggregates of late arsenopyrite (*Apy III*).

4.8. Phosphates

Apatite is by far the most common phosphate in the Panasqueira lodes and their margins, developing two main generations. The first one (*Apt I*) occurs as tiny subhedral grains in alteration haloes enriched in *Tour Ia* (\pm *Ms Ia* \pm rutile) or as corroded irregular grains in both *Ms Ia* and *Tpz Ia* selvages. The second (*Apt II*) consists of subhedral to euhedral crystals of variable dimensions, coexisting with *Ms II* and *Tpz II*.

Many other phosphates were identified in different settings, although some of them require additional work for a complete characterization due to their minute size (often smaller than the EPMA beam diameter). Considering the available dataset, it is possible to conclude that: (i) monazite grains are part of the most intense alteration haloes adjoining the quartz lodes, along with rutile or forming micrometric inclusions in *Tour Ia*; (ii) irregular inclusions of gorceixite-like (Al, Ba and F) phosphates occur in *Tpz I* and *Cst I*; (iii) small isokite-like (enriched in Ca, Mg, F \pm Na) or isoclasite-like (Ca \pm Fe²⁺,

F) grains develop along with early sulfides in OSS or form tiny inclusions in these sulfides and *Wolf I*; (iv) goyazite (Al, Sr, F \pm LREE) is common in mineral assemblages bearing *Tpz II*; (v) minor amounts of graftonite-like (Fe²⁺/Fe³⁺, Mn, Li (\pm Ca, Mg, F)) phosphates are present in coarse-grained aggregates of *Apt II*; and (vi) grains of graftonitic composition preserve rare xenotime(-Y) nano-inclusions.

4.9. Greisen-Forming Minerals

The so-called greisen-granite cupola of Panasqueira, intersected at L1, L2 and L530 of the underground mining works (see Figure 3; at L1, coordinates of the cupola centre are X = 31,945.80/Y = 54,791.68/Z = 620.0), is a fine- to medium-grained (up to 5 mm) rock mostly composed of quartz and white mica. Detailed petrography shows that the observed mineral and textural features show a series of transformations, as already noted in previous works [113,155]. The preserved primary mineral assemblage includes quartz, An₅₋₁₀ plagioclase and K-feldspar (both poorly preserved), white mica, zircon and scarce uraninite. The widespread development of albite displaying spear-shaped twins, locally enclosing relics of K-feldspar and An₁₀ plagioclase, records the progression of an early Na-metasomatism event. The secondary albite and remaining primary minerals were further disturbed by alteration processes that also led to significant deposition of interstitial quartz and white mica growth. In some secondary coarse-grained white mica flakes, the presence of hematite along cleavage surfaces and phantoms of pleochroic haloes related to metamict zircon suggest that the primary mineral assemblage should have included biotite. These late alteration processes or their continuity over time should have allowed the growth of accessory amounts of fine-grained topaz, cassiterite, arsenopyrite, sphalerite, pyrite and chalcopyrite, which occur mostly as erratic disseminations within the quartz–white mica matrix; no tourmaline was recognized in the examined samples.

5. Compositional Variation of Silicates, Oxides and Phosphates

5.1. Tourmaline

Representative analyses of each tourmaline generation (*Tour Ia*, n = 297; *Tour Ib*, n = 403; *Tour Ic*, n = 84; *Tour II*, n = 8) and the range of concentrations for essential elements are summarized in Table S2. An overview of the elemental median values for ease of reference is provided in Table 1.

Table 1. Elemental median concentration values (wt %) characterizing each tourmaline generation.

	SiO ₂	TiO ₂	Al ₂ O ₃	Fe ₂ O ₃	ZnO	FeO	MnO	CaO	MgO	Na ₂ O	Li ₂ O	F
<i>Tour Ia</i>	36.28	0.34	31.75	4.69	0.10	6.82	0.06	0.08	3.88	2.11	0.69	0.59
<i>Tour Ib</i>	36.51	0.29	31.92	4.76	0.09	5.56	0.06	0.13	4.17	2.00	0.70	0.51
<i>Tour Ic</i>	36.75	0.20	32.30	4.69	0.09	4.98	0.06	0.13	3.88	1.78	0.81	0.33
<i>Tour II</i>	37.12	0.09	31.51	6.16	0.08	1.70	0.04	0.38	5.93	2.20	0.75	0.75

Values of Fe₂O₃ and Li₂O were algebraically estimated.

According to the criteria proposed by Henry and Guidotti [156], the analyzed tourmalines plot mostly in the fields of “Li-poor granitoids and their associated pegmatites and aplites”, “metapelites and metapsammities coexisting with an Al-saturating phase”, and “metapelites and metapsammities not coexisting with an Al-saturating phase” (Figure 7a). These compositions spread largely across the “alkali-group” field, with some of them being transitional to the “vacancy-group” tourmaline (Figure 7b), scattering as well in the Al(-Li)-prevalent and Fe²⁺-dominant compositional fields, but displaying delicate differences regarding Mg and Li abundances (Figure 7c).

The compositions obtained for tourmaline are somewhat variable, showing Fe_{tot} > Mg and Na >> (K + Ca), in addition to significant F (\pm Li) contents. When in the presence of strongly zoned *Tour Ia* grains, the rims are distinctively depleted in Mg (and Ca) and enriched in Fe relative to core domains, as also noted in other studies [129,137]. Similar variations in composition at the grain scale

were documented for *Tour Ib* whenever possible for analysis with EPMA. On the contrary, *Tour Ic* and *Tour II* are more uniform in composition, being enriched in (Fe + Na) and (Mg + Ca + Li), respectively. Collectively, all these compositional variations show the contribution of several ion substitution mechanisms that are commonly implicated in tourmaline crystal chemistry and mostly affect the coordination sites A, D and Z [157]. The relevant exchanges are $(\text{Fe}^{2+})^D = (\text{Mg}^{2+})^D$, $(\text{Fe}^{3+})^D = (\text{Al}^{3+})^D$ and $(\text{Al}^{3+})^D + \square^A = (\text{R}^{2+})^D + (\text{Na}^+)^A$, confining the recorded changes to the compositional field bounded by the dravite–schorl–(Fe, Mg) foitite endmembers (Figure 7d–f).

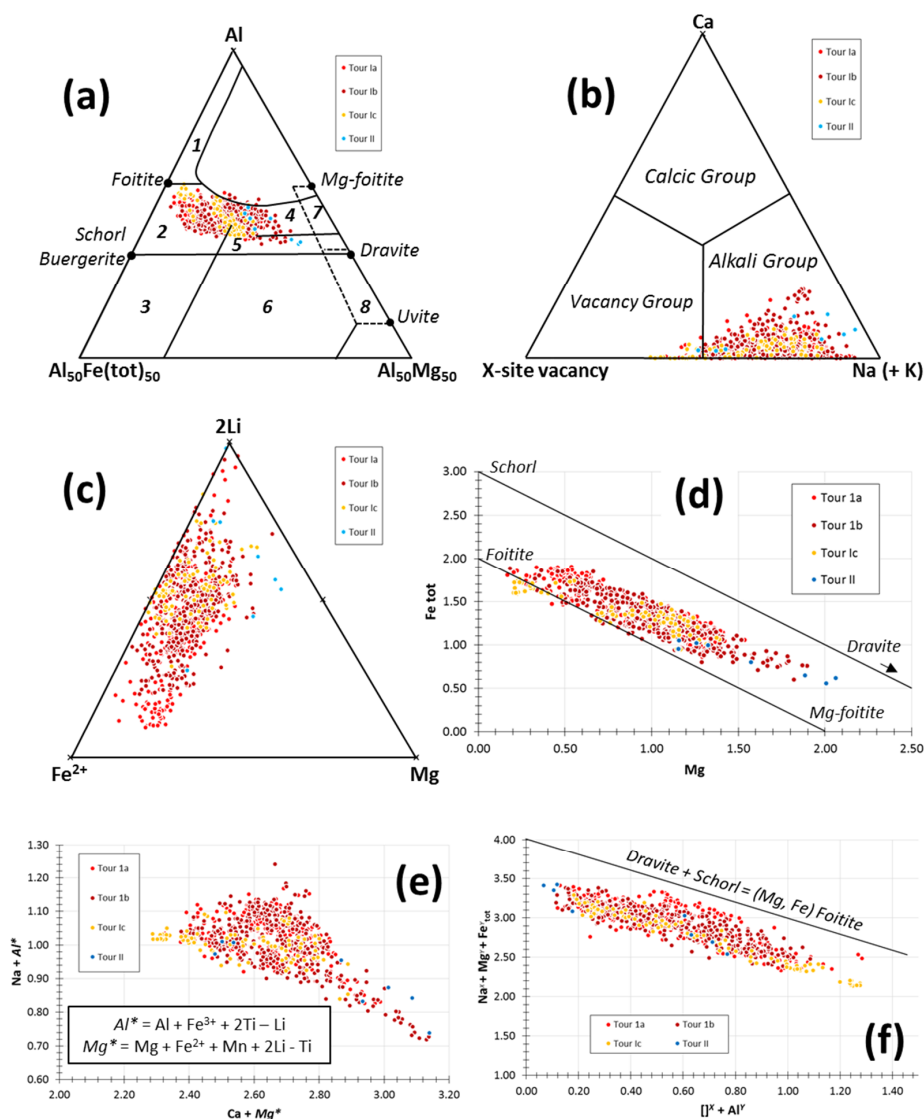


Figure 7. Ternary classification plots of tourmaline in terms of (a) Al-Fe-Mg contents [156] and (b) Ca-X-site vacancy–Na (+ K) [158]. The fields in (a) denote typical tourmaline compositions from: 1, Li-rich granitoid, pegmatite, aplites; 2, Li-poor granitoids, pegmatites, aplites; 3, Fe³⁺-rich quartz-tourmaline rocks; 4, metapelites and metapsammites with an Al-saturating phase; 5, metapelites and metapsammites without and Al-saturating phase; 6, Fe³⁺-rich quartz-tourmaline rocks, calc-silicate rocks, and metapelites; 7, low-Ca metaultramafics and Cr-, V-rich metasediments; and 8, meta-carbonates and metapyroxenites. Compositional variation of the analyzed tourmalines considering the Fe²⁺ – 2Li – Mg abundances (c). Scatter diagrams showing the predominant ion exchanges operating in these tourmalines (d–f; also see [158–160]); values in atoms per formula unit.

5.2. White Mica

Table S3 summarizes the obtained range of concentrations for essential elements and provides representative analyses for each white mica type (*Ms Ia*, n = 1326; *Ms Ib*, n = 419; *Ms Ic*, n = 164; *Ms II*, n = 162; *Ms III*, n = 62). In Table 2, an overview of the elemental median concentration values are presented for ease of reference.

Table 2. Elemental median concentration values (wt %) characterizing each white mica generation.

		SiO ₂	SnO ₂	TiO ₂	Al ₂ O ₃	Fe ₂ O ₃	Cr ₂ O ₃	FeO	MnO
<i>Ms Ia</i>	Subgroup 1 (n = 607)	46.36	0.07	0.11	29.73	-	0.05	3.63	0.06
	Subgroup 2 (n = 178)	47.54	-	0.16	30.91	2.59	0.06	0.74	0.04
	Subgroup 3 (n = 109)	48.13	0.02	0.12	25.81	-	0.06	4.59	0.04
	Subgroup 4 (n = 284)	47.46	0.03	0.14	31.24	-	0.06	3.23	0.06
	Subgroup 5 (n = 37)	54.44	-	0.02	25.35	-	0.06	2.18	0.03
<i>Ms Ib</i>	Subgroup 1 (n = 360)	48.44	-	0.08	30.32	-	0.06	3.59	0.06
	Subgroup 2 (n = 19)	49.78	-	0.04	21.26	-	0.07	8.45	0.05
	Subgroup 3 (n = 40)	47.00	-	0.06	32.04	-	0.06	3.04	0.06
<i>Ms Ic</i>		48.30	0.05	0.20	30.11	-	0.06	2.77	0.06
<i>Ms II</i>	Subgroup 1 (n = 135)	48.84	-	0.10	29.31	-	0.06	3.08	0.05
	Subgroup 2 (n = 25)	47.76	-	0.11	30.64	-	0.06	3.12	0.06
<i>Ms III</i>		54.92	-	-	25.12	-	0.05	2.07	0.02
		BaO	CaO	MgO	Cs ₂ O	K ₂ O	Na ₂ O	Li ₂ O	F
<i>Ms Ia</i>	Subgroup 1 (n = 607)	0.05	0.02	1.00	-	10.62	0.24	-	1.61
	Subgroup 2 (n = 178)	0.05	0.02	1.07	-	11.99	0.40	-	1.42
	Subgroup 3 (n = 109)	0.04	0.03	1.50	-	10.54	0.10	3.68	2.30
	Subgroup 4 (n = 284)	0.05	0.01	0.66	-	11.03	0.42	1.39	1.39
	Subgroup 5 (n = 37)	0.02	0.32	2.18	-	9.26	0.03	-	1.51
<i>Ms Ib</i>	Subgroup 1 (n = 360)	0.04	0.02	0.88	-	10.70	0.27	-	1.57
	Subgroup 2 (n = 19)	0.04	0.02	-	0.01	10.38	0.05	3.53	4.10
	Subgroup 3 (n = 40)	0.03	0.01	0.43	-	11.00	0.50	1.38	1.23
<i>Ms Ic</i>		0.18	0.02	1.36	-	10.78	0.28	-	-
<i>Ms II</i>	Subgroup 1 (n = 135)	0.03	0.02	1.56	-	10.77	0.23	-	1.89
	Subgroup 2 (n = 25)	0.07	0.01	0.78	-	11.15	0.35	1.70	1.17
<i>Ms III</i>		0.02	0.32	3.35	-	9.12	0.03	-	1.50

Values of Fe₂O₃ and Li₂O were algebraically estimated.

A close inspection of the EPMA data shows that several white mica generations may be further subdivided according to petrographic and compositional criteria. Regarding *Ms Ia*, subgroup 1 includes analyses of large mica plates in thick selvages enriched in tourmaline and subgroup 2 comprises analyses of coarse-grained micas in thinner selvages bearing accessory tourmaline and topaz, whereas subgroups 3 and 4 assemble analyses of rims of the large micas of subgroup 1 and of the micas forming subgroup 2, respectively; subgroup 5 documents local compositional readjustments affecting *Ms Ia* crystals (mainly belonging to subgroup 1) during a late alteration event. Summing up the whole analytical dataset for *Ms Ia*, it becomes clear that micas forming different selvage types (subgroups 1 and 2) are enriched in F and characterized by distinct FeO/MgO, FeO/Fe₂O₃ and K₂O/Na₂O proportions. Their minor constituents (Cr, Mn, Ba, Ca) are similar, excluding Sn, which was only detected in subgroup 1. The edge domains of mica plates from both subgroups also display distinctive Mg and Na contents, however with comparable enrichments in Li (algebraically estimated on the basis of charge balances) and traces of Sn. Late alteration processes led to evident depletion of K (\pm Na), along with an increase in Si (\pm Ca).

Ms Ib analyses constitute 3 different subgroups: subgroup 1 comprises analyses of the common fine-grained non-oriented micas within discontinuous borders of quartz lodes; subgroup 2 includes analyses of mica grains in thin bands bearing accessory *Tour Ic* and *Tpz Ib*; and subgroup 3 collects analyses of *Ms Ib* micas in fractures criss-crossing *Ms Ia* selvages and a few comparable analyses of micas occurring in greisen samples. Briefly, *Ms Ib* shares some compositional features with *Ms Ia*, but presents somewhat different FeO/MgO and K₂O/Na₂O proportions, along with distinct minor or trace fingerprints. In *Ms Ib*, Ti never attains concentration values typical of a minor constituent and Sn abundances are always below the EPMA detection limit. The composition of *Ms Ib* Fe-rich micas included in subgroup 1 only roughly compares with that found in transitional core–border domains of large *Ms Ia* plates. Micas forming the subgroup 2 of *Ms Ib* display Li concentrations comparable to those characterizing the edges of large mica plates in lode selvages (subgroup 3 of *Ms Ia*), but their trace amounts of Cs appear to be a distinct feature. Subgroup 3 of *Ms Ib* is compositionally analogous to the rims of micas included in subgroup 4 of *Ms Ia*, although differing in Ti and Sn abundances.

No meaningful subdivision of *Ms Ic* is possible. Apart from its tendency to incorporate higher amounts of Ba, *Ms Ic* does not display any other distinctive compositional feature in comparison with other micas developed during OSS, for which Fe²⁺ > Mg and no Fe³⁺ or Li are algebraically required to ensure the global charge balance.

Two distinct *Ms II* subgroups were recognized on the basis of EPMA results. Subgroup 1 contains most of the analyses of grains belonging to this white mica generation; subgroup 2 is a small group of analyses which is characterized by its higher Li contents, interpreted as an early composition fingerprint in the context of *Ms II*. Therefore, the main difference between *Ms II* and micas grown throughout OSS appears to be its tendency towards F-enriched compositions, possibly along with a gradual increase in Mg (and decreased Li), but without change in the Fe > Mg disproportionation.

The composition of *Ms III* is comparable to the one showing local alteration of *Ms Ia* (subgroup 5), despite the distinctively lower FeO/MgO proportion and lower amounts of trace components and not including any contribution of Ti.

Considering the whole analytical dataset for white micas, some fundamental key features readily emerge. All these micas incorporate significant amounts of F and their compositions show strong to very strong deviations from ideal muscovite towards the ferroaluminoceladonite endmember (Figure 8a). When bearing Li, the ferroaluminoceladonite compositions deviate towards the polyolithionite endmember (i.e., Li-Fe group); this is the case for subgroups 3 and 4 of *Ms Ia*, 2 and 3 of *Ms Ib* and 2 of *Ms II*. Some of the most important compositional features displayed by the analyzed micas can also be compared on the basis of their (Na₂O + Li₂O), (FeO + Fe₂O₃) and (MgO + MnO) abundances, as illustrated in Figure 8b, separating Li-bearing micas and many *Ms Ia* analyses from the remaining subgroups. However, additional evidence supporting the intended comparison came from the analysis of ion substitution mechanisms accounting for the incorporation of R²⁺ ions in dodecahedral coordination sites (ideally occupied by R⁺), and of R⁺, R²⁺ and R⁴⁺ ions in octahedral coordination sites (replacing Al³⁺ or partly filling the vacancies typical of dioctahedral micas) affecting the Si/Al proportions in tetrahedral coordination [157,161–165].

Simple ion interchanges acting over dodecahedral sites (*xii*), (K⁺)^{*xii*} = (R⁺)^{*xii*} (mostly Na⁺) are variably complemented by those accounting for the incorporation of (R²⁺)^{*xii*} (usually Ca and Ba). The latter preferentially involve the mechanism (R⁺)^{*xii*} + (Al³⁺)^{*vi*} = (R²⁺)^{*xii*} + (R²⁺)^{*vi*}, except in micas forming the subgroup 5 of *Ms Ia* and *Ms III* (Figure 9a), for which the incorporation of R²⁺ in *xii* positions is better explained through the interchange (R⁺)^{*xii*} + (Si⁴⁺)^{*iv*} = (R²⁺)^{*xii*} + (Al³⁺)^{*iv*}. Additionally, the increase of *xii* vacancies along with (Si⁴⁺)^{*iv*} contents in *Ms Ia* and *Ms III* micas reveals that the (Al³⁺)^{*iv*} + (R⁺)^{*xii*} = (Si⁴⁺)^{*iv*} + □^{*xii*} exchange also plays a significant role.

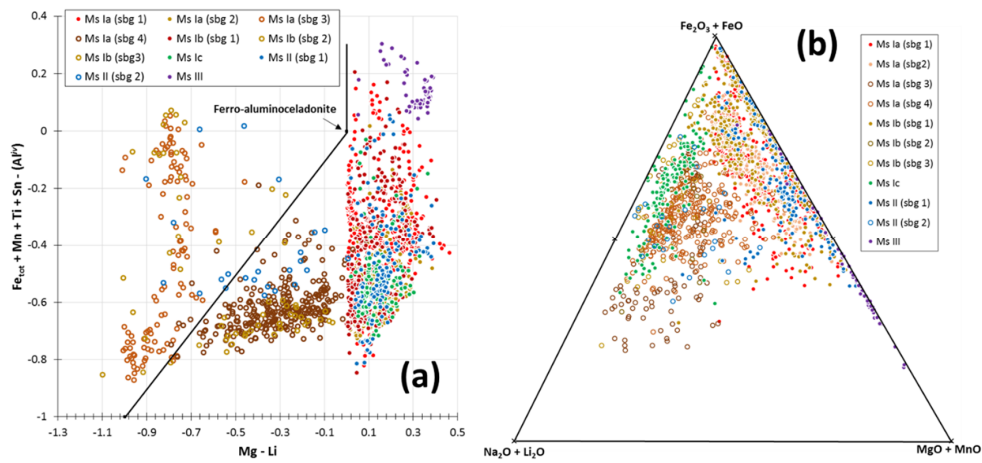


Figure 8. (a) Position of the analyzed micas in the *mgli* vs. *feal* diagram [163] and (b) in the ternary plot $(Na_2O + Li_2O) - (FeO + Fe_2O_3) - (MgO + MnO)$.

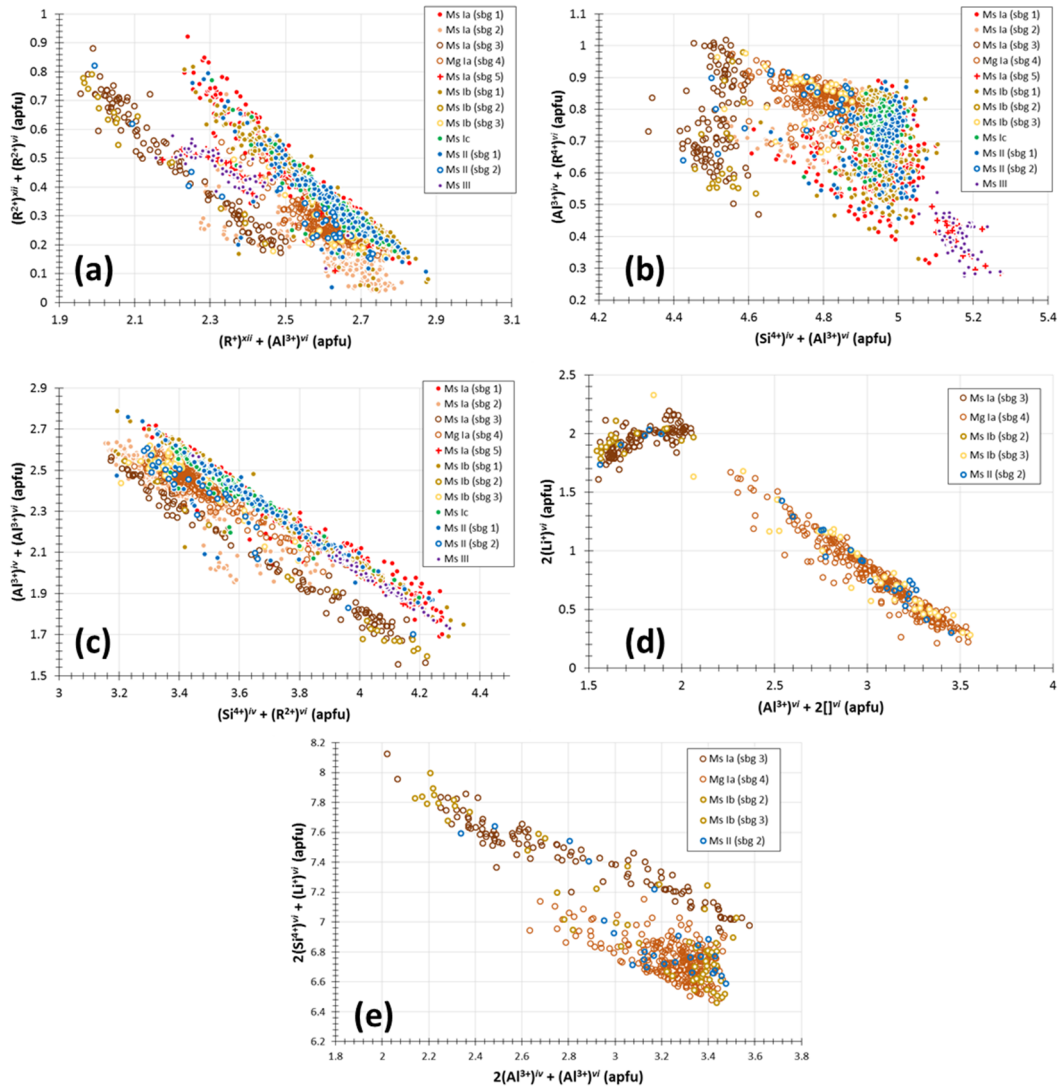


Figure 9. Cross-plots of atoms per formula unit (apfu) in different coordination sites documenting the prevailing substitution mechanisms in the analyzed mica groups and subgroups, as indicated in text for each case, from (a–e).

In octahedral coordination sites (*vi*), a large number of ion interchange mechanisms exist. Trivial exchanges involve the replacement of $(Al^{3+})^{vi}$ by other R^{3+} ions (often Fe^{3+} or Cr^{3+}), but these only assume key importance in subgroup 2 of *Ms Ia*, where overall stoichiometric constraints show that part of the analyzed iron should be ferric for a statistically relevant number of analyses. The exchange $(Al^{3+})^{vi} = R^{4+}$ (Ti, Sn) is also minor and quite irregular, mostly ruled by the $(Al^{3+})^{vi} + (Si^{4+})^{iv} = (R^{4+})^{vi} + (Al^{3+})^{iv}$ mechanism (Figure 9b). On the contrary, the incorporation of R^{2+} (Fe^{2+} , Mg, Mn) is extensive, mostly substituting $(Al^{3+})^{vi}$ in agreement with the Tschermak mechanism (TK), $(Si^{4+})^{iv} + (R^{2+})^{vi} = (Al^{3+})^{iv} + (Al^{3+})^{vi}$ (Figure 9c). However, for many analyses, the total of $(R^{2+})^{vi}$ is not suitably explained only by the TK interchange, recording a partial use of octahedral vacancies as $3(R^{2+})^{vi} = 2(Al^{3+})^{vi} + \square^{vi}$. The occupancy of these vacancies is, however, much more significant whenever the overall stoichiometric constraints strongly suggests the presence of Li. This is the case for subgroup 4 of *Ms Ia* and subgroup 3 of *Ms Ib*, along with a few cases included in subgroup 2 of *Ms II*, for which the incorporation of Li should be regulated by the exchange $(Al^{3+})^{vi} + 2\square^{vi} = 3(Li^{+})^{vi}$ (Figure 9d). For the remaining Li-bearing micas, in particular those forming the subgroups 3 and 2 of *Ms Ia* and *Ms Ib*, the charge imbalance justifying the presence of Li is different and the incorporation of this element should be ruled mainly by the coupled substitution mechanism $2(Al^{3+})^{iv} + (Al^{3+})^{vi} = 2(Si^{4+})^{iv} + (Li^{+})^{vi}$ (Figure 9e).

5.3. Topaz

The ranges of concentrations for essential constituents and representative analyses of each topaz generation (*Topz Ia*, $n = 225$; *Topz Ib*, $n = 287$; *Topz II*, $n = 80$) are presented in Table S4. In Table 3, an overview of the elemental median concentration values are presented for ease of reference.

Table 3. Elemental median concentration values (wt %) characterizing each topaz generation.

	Ta ₂ O ₅	Nb ₂ O ₅	SiO ₂	Sm ₂ O ₃	Nd ₂ O ₃	Pr ₂ O ₃	Ce ₂ O ₃	La ₂ O ₃	Fe ₂ O ₃	Al ₂ O ₃	ZnO	F
Topz Ia	0.01	-	32.27	0.01	0.02	0.04	0.02	-	0.04	54.95	0.02	13.42
Topz Ib	0.02	-	32.30	-	-	0.04	-	-	0.02	54.88	0.02	13.42
Topz II	0.04	0.02	32.23	-	-	0.04	0.02	0.01	0.02	54.86	-	13.49

Values of Fe₂O₃ were algebraically estimated.

Topz Ia, *Ib* and *II* are distinguishable only because of their minor and trace element signatures. Iron and praseodymium are always present, but zinc is absent from *Topz II* and cerium is absent from *Topz Ib*. Neodymium and samarium appear to be exclusive of *Topz Ia*, barium of *Topz Ib*, and niobium and lanthanum of *Topz II*. Therefore, ion exchange mechanisms related to the incorporation of small amounts of different R^{2+} , R^{3+} and R^{5+} ions affect the coordination positions ideally occupied by Al^{3+} (A). However, mechanisms other than $Al^{3+} = R^{3+}$ ($= Fe^{3+}$, REE) are required to restore the charge imbalance caused by the substitution of Al^{3+} by R^{2+} or R^{5+} [166]. The $3(Al^{3+})^A = (R^{5+})^A + 2(R^{2+})^A$ interchange, although conceptually possible, does not fit the available analytical data (Figure S1a in Supplementary Materials). Therefore, the incorporation of R^{2+} and R^{5+} should have been assisted by coupled substitution mechanisms involving T and A positions, such as $(Si^{4+})^T + 2(R^{3+})^A = (Al^{3+})^T + (R^{5+})^A + (R^{2+})^A$ (Figure S1b) and $(Si^{4+})^T + (R^{2+})^A = (Al^{3+})^T + (R^{3+})^A$ (Figure S1c), which acting together lead to the general exchange $2(Si^{4+})^T + (R^{3+})^A = 2(Al^{3+})^T + (R^{5+})^A$.

5.4. Chlorite

The concentration ranges for essential elements, together with representative analyses of each chlorite generation (*Chl I*, $n = 273$; *Chl II*, $n = 222$; *Chl III*, $n = 216$), are concisely reported in Table S5. In Table 4, an overview of the elemental median concentration values are presented for ease of reference.

EPMA data show that all chlorite generations are chemically inhomogeneous and that each of them can be divided in two different subgroups. For *Chl I*, subgroup 1 is composed of chlorite grains surrounding *Ms Ic* aggregates, whereas subgroup 2 gathers analyses of *Chl I* filling fractures affecting

Wolf I aggregates. For *Chl II*, subgroup 1 documents chlorite grains surrounding *Ms II* or *Tpz II* and subgroup 2 pertains to analyses of chlorite enclosing sulfide aggregates. A somewhat similar situation is also found in *Chl III*, whose subgroup 1 represents analyses from *Chl III* dense masses in contact with carbonates (mainly siderite) or loose crystals in thin fracture infillings away from sulfide grains, while subgroup 2 is composed of those analyses performed on grains adjoining sulfides.

Table 4. Elemental median concentration values (wt %) characterizing each chlorite generation.

		SiO ₂	Cr ₂ O ₃	Al ₂ O ₃	ZnO	FeO	MnO	MgO	F
<i>Chl I</i>	Subgroup 1 (n = 95)	23.32	0.07	20.89	0.03	42.95	0.11	1.23	0.13
	Subgroup 2 (n = 178)	23.42	0.07	20.25	0.02	44.55	0.10	0.67	0.12
<i>Chl II</i>	Subgroup 1 (n = 95)	25.08	0.06	22.26	-	36.17	0.05	4.58	0.08
	Subgroup 2 (n = 44)	24.01	0.07	19.79	-	44.08	0.13	0.66	0.10
<i>Chl III</i>	Subgroup 1 (n = 182)	25.21	0.07	20.97	0.03	42.95	0.15	2.60	0.06
	Subgroup 2 (n = 34)	24.92	0.07	21.18	0.03	43.73	0.10	0.79	0.05

Considering the whole analytical dataset gathered for chlorite, the primacy of Fe over Mg is evident. The assortment of trace elements does not significantly disturb the documented deviations from the chamosite (Chm) endmember towards Fe-amesite (Fe-Am) and sudoite (Sud) compositions (Figure 10a). Accordingly, the compositional variation of chlorite is basically explained by the combination of the following ion exchange mechanisms (Figure 10b,c) [167–171]: $(Fe^{2+})^{vi} = (Mg^{2+})^{vi}$, $(Si^{4+})^{vi} + (R^{2+})^{vi} = (Al^{3+})^{iv} + (Al^{3+})^{vi}$ and $3(R^{2+})^{vi} = 2(R^{3+})^{vi} + \square^{vi}$, where R^{2+} accounts for any divalent ion (Fe^{2+} , Mg, Mn, Zn, Ni) incorporated in octahedral coordination positions (vi) at the expense of R^{3+} (mostly Al) partitioning between octahedral and tetrahedral (iv) sites or of octahedral vacancies (\square^{vi}). In addition, a limited substitution of (OH)- by F- should also be considered.

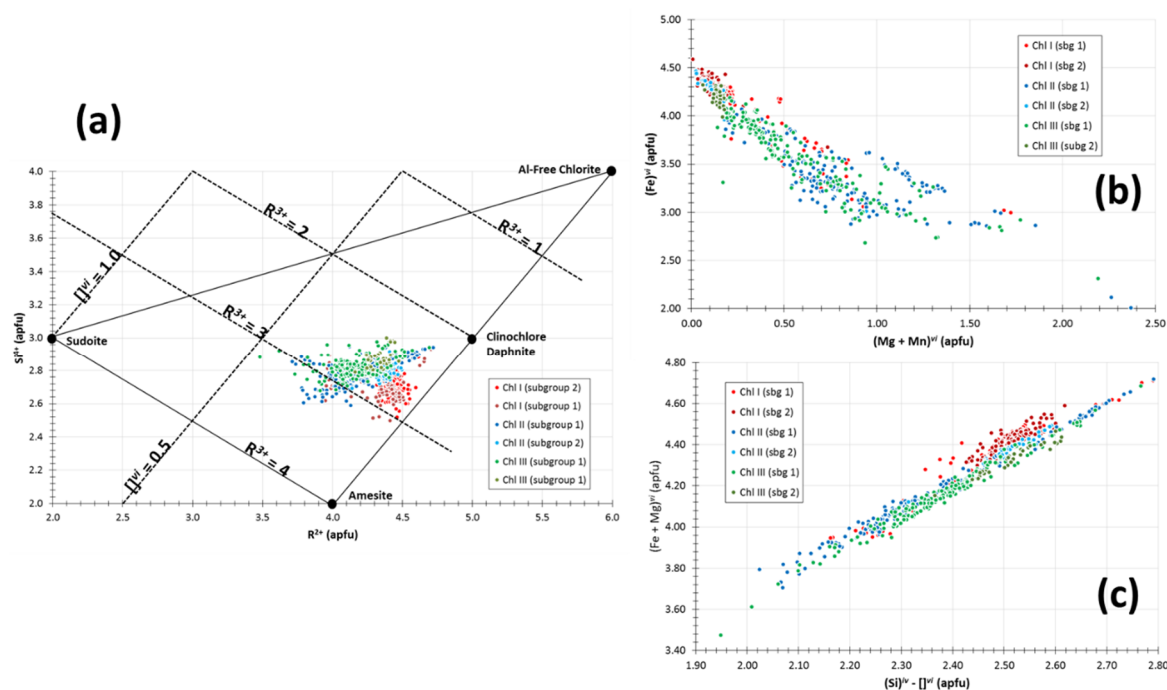


Figure 10. (a) Position of the analyzed chlorite in the R^{2+} vs. Si^{4+} diagram [169]; apfu = atoms per formula unit. Cross-plots (b) and (c) documents of the predominant exchange mechanisms operating in these chlorites.

5.5. Rutile

A total of 130 quantitative analyses were performed in rutile grains within tourmaline-rich mineral assemblages and topaz selvages bearing cassiterite. In the former subgroup, analyses representing patchy cores were separated from those characterizing well-defined rims whenever suitably resolved with EPMA electron backscattered images; when impossible to guarantee such separation, the data were processed without any particular labelling. Table S6 summarizes the concentration ranges for essential elements along with representative analyses of rutile. An overview of the elemental median concentration values are presented in Table 5 for ease of reference.

Table 5. Elemental median concentration values (wt %) characterizing rutile grains.

WO ₃	Ta ₂ O ₅	Nb ₂ O ₅	SnO ₂	ZrO ₂	TiO ₂	Fe ₂ O ₃	Cr ₂ O ₃	V ₂ O ₃
1.57	0.04	0.26	1.69	0.02	93.87	1.01	0.04	0.30

A detailed inspection of the analytical dataset reveals that the composition varies considerably within a single rutile grain or between rutile grains representing different textural frameworks. The composition of rutile in tourmaline-rich assemblages is quite heterogeneous and the grain cores are distinctly enriched in Nb, Ta and V (\pm Fe). The rims of these grains show a tendency to incorporate higher W contents, as observed in optically homogeneous rutile within topaz selvages. Concentrations of Sn fluctuate extensively, but the resulting enrichment or depletion patterns are rather irregular. Variations in Zr and Cr abundances are, on the contrary, fairly limited and independent of both the intragrain context and rutile-bearing mineral assemblage. Accordingly, a general trend for rutile composition could be outlined in the (Nb + Ta) – (W + Sn) – (Fe + V + Cr) diagram (Figure S2a in Supplementary Materials), despite the uncertainties related to the impossibility of ascribing all data point analyses to a particular domain of each grain. Plotted in the $100 \times (\text{Fe}_2\text{O}_3 + \text{Cr}_2\text{O}_3 + \text{V}_2\text{O}_3) - \text{TiO}_2 - 1000 \times \text{WO}_3$ diagram (Figure S2b), these compositions also define an evident trend identical to those expected for granite-related ore-forming systems [172]. The obtained results are fully consistent with recently published data [138], although differing in some details due to the resolution and accuracy of the analytical techniques employed.

The rutile composition is quite heterogeneous, showing (variable and not linearly co-variant) minor amounts of Sn, W and Fe, often occurring along with traces of Nb (\pm Ta), V (\pm Cr) and Zr. Therefore, the prevailing mechanisms of Ti substitution should account for other R⁴⁺ cations (Sn and Zr), besides R⁶⁺ (W), R⁵⁺ (Nb and Ta) and R³⁺ (Fe, V and Cr) [173]. Charge balance considerations make $\text{Ti}^{4+} = \text{R}^{4+}$, $3\text{Ti}^{4+} = 2\text{R}^{3+} + \text{R}^{6+}$ and $2\text{Ti}^{4+} = \text{R}^{3+} + \text{R}^{5+}$ the most plausible ion exchange mechanisms; jointly, they yield $6\text{Ti}^{4+} = \text{R}^{6+} + \text{R}^{5+} + \text{R}^{4+} + 3\text{R}^{3+}$ and explain the compositional variability of rutile in Panasqueira, as illustrated in Figure S2c.

5.6. Cassiterite

The concentration ranges for essential elements and representative analyses of *Cst I* (n = 615), *Cst II* (n = 337) and *Cst_g* (n = 5) are listed in Table S7. An overview of the elemental median concentration values are presented in Table 6 for ease of reference.

Table 6. Elemental median concentration values (wt %) characterizing *Cst I* and *Cst II*.

	WO ₃	SnO ₂	TiO ₂	Fe ₂ O ₃	Cr ₂ O ₃	V ₂ O ₃	ZnO
<i>Cst I</i>	0.02	98.95	0.51	0.03	0.02	0.01	0.03
<i>Cst II</i>	-	99.05	0.44	0.03	0.01	0.01	0.03

The optical zonation often observed in *Cst I*, sometimes displaying strong contrasting features, is not correlated with significant compositional variations detectable on the basis of EPMA results.

As in *Cst II*, the $\text{Sn}^{4+} = \text{Ti}^{4+}$ ion interchange accounts for most of the documented deviations from ideal SnO_2 (Figure S3a in Supplementary Materials). However, substitution mechanisms involving R^{2+} , R^{3+} , R^{5+} and R^{6+} ions should not be discarded [174–177], mainly when Ti contents are quite low, as happens in numerous cases. In these circumstances, the contribution of R^{6+} (= W) and R^{3+} (mostly Fe^{3+}) for the compositional variation of cassiterite appears to be more relevant in *Cst I*, whereas the incorporation of R^{5+} (Ta > Nb) and R^{2+} (usually Zn, Cu, Ni, Co) is noteworthy in *Cst II*. Accordingly, the substitution mechanisms $2\text{Sn}^{4+} = \text{W}^{6+} + 2/3\text{R}^{3+} + 1/3\Box$ and $3\text{Sn}^{4+} = 2(\text{Nb, Ta})^{5+} + \text{R}^{2+}$ must be added to the prevalent $\text{Sn}^{4+} = \text{Ti}^{4+}$ interchange, resulting in the general balance of $6\text{Sn}^{4+} = \text{Ti}^{4+} + \text{W}^{6+} + 2(\text{Nb, Ta})^{5+} + 2/3\text{R}^{3+} + \text{R}^{2+} + 1/3\Box$ (Figure S3b).

5.7. Wolframite

Representative analyses and concentration ranges for essential elements in wolframite grains (*Wolf I*, $n = 665$; *Wolf II*, $n = 476$) are summarized in Table S8. An overview of the elemental median concentration values are presented in Table 7 for ease of reference.

Table 7. Elemental median concentration values (wt %) characterizing each wolframite generation.

	WO_3	Nb_2O_5	ZrO_2	Bi_2O_3	Fe_2O_3	ZnO	NiO	CoO	FeO	MnO
<i>Wolf I</i>	75.09	0.23	0.02	0.02	1.89	0.04	0.01	0.02	18.52	3.77
<i>Wolf II</i>	75.21	0.25	0.01	0.02	1.66	0.03	0.01	0.03	18.72	3.64

Values of Fe_2O_3 were algebraically estimated.

The compositional variation of wolframite from Panasqueira is basically explained by the $\text{Fe}^{2+} = \text{Mn}^{2+}$ interchange (Figure S4a in Supplementary Materials) and a coupled substitution mechanism involving the positions ideally occupied by (Fe, Mn) and W, accounting for the incorporation of R^{3+} ions (mostly Fe^{3+} , but also sporadic Cr and V) [176,178]: $1/3(\text{R}^{3+})^T + (\text{Fe}^{3+})^M = 1/3(\text{W}^{6+})^T + (\text{Fe}^{2+}, \text{Mn}^{2+})^M$. Assuming that Zn, Ni and Co traces replace $(\text{Fe}^{2+}, \text{Mn}^{2+})^M$, the latter mechanism can be re-written as $1/3(\text{R}^{3+})^T + (\text{Fe}^{3+})^M = 1/3(\text{W}^{6+})^T + (\text{R}^{2+})^M$; indeed, the inclusion of these minor cations in the plot improves the inverse linear relationship implicated by the ionic and charge balances (Figure S4b).

Additional substitution mechanisms must be considered to explain the incorporation of minor amounts of R^{5+} (Nb >> Ta) and R^{4+} (Zr > Ti >> Si) ions, conceivably exchanging with W^{6+} [176,178]. Most plausible are the coupled ion exchanges expressed as $(\text{R}^{5+})^T + (\text{R}^{3+})^M = (\text{W}^{6+})^T + (\text{Fe}^{2+})^M$ and $(\text{R}^{4+})^T + (\text{R}^{2+})^M = (\text{W}^{6+})^T + \Box^M$, which can be taken together as $(\text{R}^{5+})^T + (\text{R}^{4+})^T + (\text{R}^{3+})^M = 2(\text{W}^{6+})^T + \Box^M$ (Figure S4c). These ion exchanges, although minimal, are meaningful and provide evidence for irregular Nb (\pm Ta) and Zr (\pm Ti) enrichments in many core domains of *Wolf I* and *Wolf II* (Figure S4d,e).

5.8. Uraninite

Five uraninite grains found in the examined samples of the greisen-granite cupola were analyzed (Table S9). Three of them, being coarser in size (up to 30 μm), represent interstitial uraninite at the interface of primary quartz and secondary white mica; the other two exemplify minute ($\approx 10 \mu\text{m}$) grains included in secondary coarse-grained white mica (Figure S5a,b in Supplementary Materials). Both sets of analyses showed measurable concentrations of PbO, ranging from 3.7 to 3.9 wt %. On the contrary, thorium was only detected in interstitial uraninite, for which the ThO_2 abundances vary between 0.5 and 1.9 wt %. Accordingly, the compositional variation of the analyzed uraninite grains is fully described by the usual substitution mechanism $\text{U}^{4+} = (\text{Th, Pb})^{4+}$. In addition, and considering the iterative calculation method reported in literature [179,180], average ages of $\approx 298 \pm 2$ Ma and $\approx 283 \pm 2$ Ma can be estimated for these two groups of uraninite, respectively.

5.9. Apatite

A summary of the available data and of representative compositions of apatite (*Apt I*, $n = 131$; *Apt II*, $n = 433$) is listed in Table S10. An overview of the elemental median concentration values is provided in Table 8 for ease of reference.

Table 8. Elemental median concentration values (wt %) characterizing each apatite generation.

	REE ₂ O ₃	Fe ₂ O ₃	Mn ₂ O ₃	P ₂ O ₅	SrO	FeO	MnO	CaO	MgO	Na ₂ O	Cl	F
<i>Apt I</i>	0.11	0.20	0.04	41.98	0.03	-	-	54.24	0.01	0.06	0.01	3.34
<i>Apt II</i>	0.08	-	-	42.75	0.14	0.21	1.03	54.25	0.01	0.03	0.01	3.33

Values of Fe₂O₃ and Mn₂O₃ were algebraically estimated.

The replacement of Ca by other divalent cations ($R^{2+} = \text{Sr, Fe}^{2+}, \text{Mg or Mn}$) is relevant in both generations of apatite (Figure 11a). However, the expected negative linear relationship between total R^{2+} and P is significantly disturbed for *Apt I* analyses (Figure 11b). Therefore, substitutions implicating R^{3+} ($= \text{Fe}^{3+} + \text{REE}$) must be considered for this group of analyses [181–185]. In this regard, the most plausible mechanism to explain the incorporation of R^{3+} in *Apt I* is $\text{P}^{5+} + (\text{R}^{2+})^M = (\text{R}^{3+})^M + \text{Si}^{4+}$, despite the occurrence of some data scattering (Figure 11c), which clearly reflects the significant variability of the measured Si contents (most often below the EPMA detection limit). Note that no meaningful contents of B, S, V or As were detected.

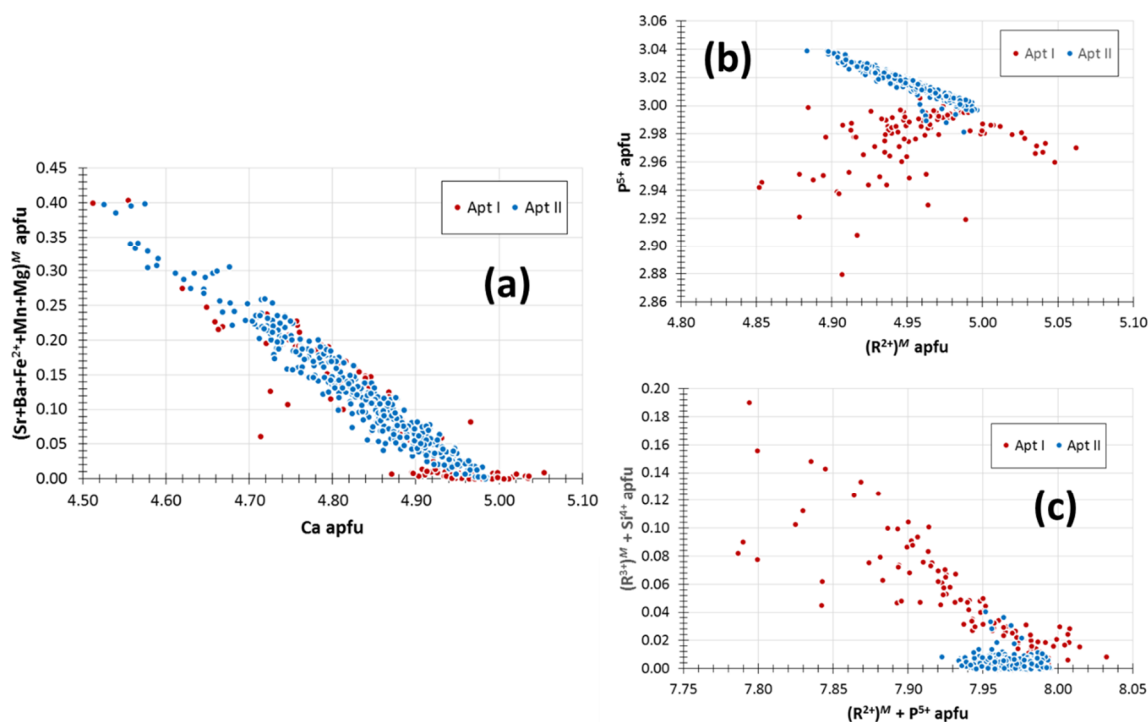


Figure 11. Compositional variations of *Apt I* and *Apt II* documenting the usual replacement of Ca by other divalent cations ($R^{2+} = \text{Sr, Ba, Fe}^{2+}, \text{Mg or Mn}$), as discussed in text (a,b), besides the relative importance of substitutions involving R^{3+} ($= \text{Fe}^{3+} + \text{REE}$) (c).

6. Discussion

Systematic observations made in underground works spreading across all the accessible sectors of the Panasqueira mine, further complemented by the examination of a wide range of samples, show that mineral infillings of quartz lodes are quite diverse. Even so, using as criteria the mineral assemblages forming the lode borders and the relative abundance of prevalent oxides (wolframite and cassiterite),

four main geological trends can be distinguished (Figure 12). Adjoining the greisen-granite cupola and immediately to the S–SW of its location, the lodes are regularly bordered by thick *Ms Ia* selvages comprising *Tour Ia*, and *Wolf I* prevails over *Cst I*. Further SSW, far from the cupola, lode borders are most commonly outlined by thin (often discontinuous) bands of *Ms Ib* (\pm *Tour Ib* and *Tpz Ib*), and *Wolf I* came along with accessory (and fine-grained) *Cst I* whenever the latter oxide is present. To the west of the cupola, *Ms Ia* selvages of considerable thickness also form the edges of the most characteristic lodes, but they are gradually enriched in *Tpz Ia* and *Cst I* as the distance to the cupola increases, which is roughly coupled by a gradual decreasing of *Tour Ia* (in abundance and grain size) and *Wolf I*. In the SW sector of the mine, far from the greisen-granite cupola, the lodes are typically bordered by thick *Tpz Ia* selvages where *Cst I* (+ rutile) largely predominates over *Wolf I*. These geological trends, although disregarding many other relevant features related to the main stage of sulfide deposition in quartz lodes, are also consistent with the spatial distribution of tungsten or high-grade tin domains of the lode swarm mined in previous years. Therefore, they provide a plausible first approach for the establishment of an exploratory mineral and geochemical zonation at the mine scale.

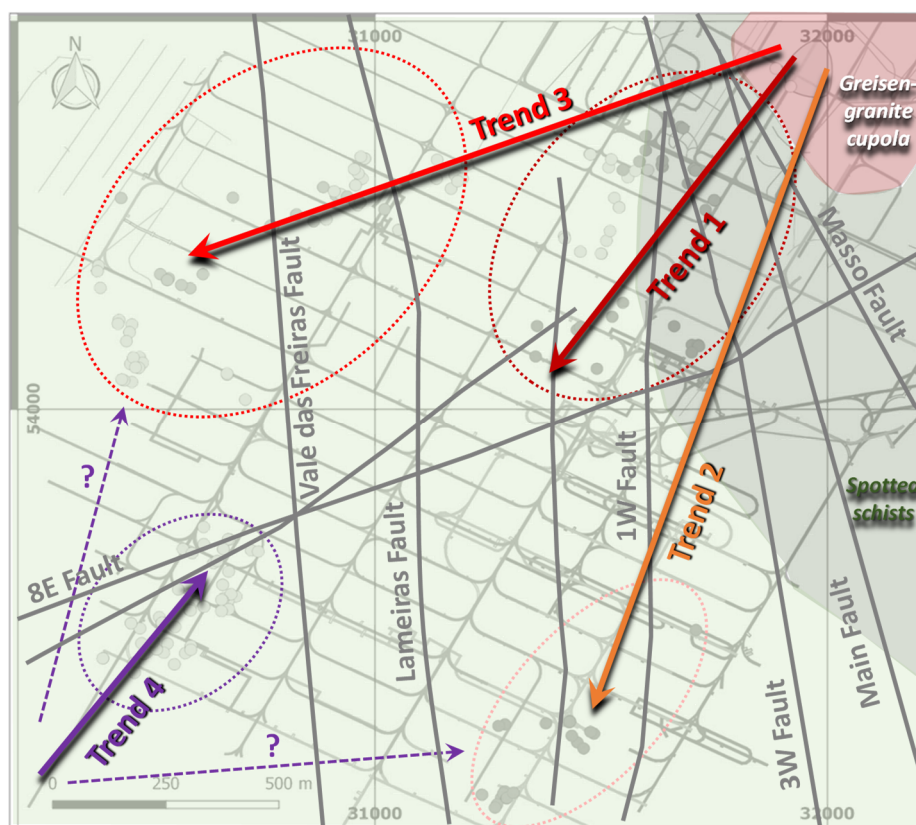


Figure 12. Schematic illustration of the geological trends at the mine scale discussed in the text, using as the background the simplified map shown in Figure 2. Dashed ellipses encircle different sample sets (see Figure 3 for details).

Additional evidence supporting the inference of the aforementioned four geological trends comes from microscale analysis of quartz lode walls and detailed characterization of contacts with country metasedimentary rocks. In fact, the mineralogical and geochemical features typical of each trend are indirectly controlled by the cyclic permeability renewal, which did not occur evenly at the mine scale. This explains why the evolving path preceding the main stages of quartz lode development is not the same in each geological trend, although several features are shared in some cases. One key factor to explain such differences is the competency contrast between pelitic and psamitic sediments, which under equivalent stress fields generates distinct arrays of connected microfractures ruling the intensity

of tourmalinization in country rocks and the subsequent growth of larger structures. Another decisive factor is the recurrence of fluid flow into fractured rock domains, locally reinforcing the alteration haloes or leaving a record of successive cycles of permeability renewal and sealing by somewhat different mineral assemblages. A third critical factor concerns the role of fluid overpressure during consecutive stages of lode formation, determining its (re)opening [118,120,121,133,186]. The longest records of these cycles are preserved around and along the walls of many thick quartz lodes with *Ms Ia* selvages found in the northern sectors of the mine: evident in quartz lodes situated close to the greisen-granite cupola (first trend), but also in various similar structures located to the west (third trend). These records comprise the early formation (previous to *Ms Ia* selvages) of cracks sealed with *Tour Ia* + rutile (\pm monazite), later followed by microfractures showing different mineral infillings: sulfides *Ia*, affecting *Wolf I*; *Ms Ib*, criss-crossing *Ms Ia* selvages; and *Tour Ic*. Thus, the initial steps of quartz lode development at Panasqueira should have involved a series of fracturing events favoring the flow of multiple, and possibly short-lived, fluid pluses. This being so, and accepting the reported criteria for the first two geological trends, the mineralization onset in domains placed to the SSW of the greisen-granite cupola should have occurred after the time window during which *Ms Ia* selvages grew in structures that are quite well-represented near that cupola and immediately to the S-SW of it. Furthermore, the distinct features presented by lode walls with thick *Tpz Ia* selvages strongly suggests that the beginning of ore-forming in the SW sector of the mine should have caused the inflow of fluids of different composition. This opens the possibility of having a second source of mineralizing fluids to the SW related to an outgrowth of the (voluminous) batholith, which also created the known cupola, or to a distinct granite body. If so, the relative enrichment in topaz (\pm cassiterite) in *Ms Ia* or *Ms Ib* selvages of quartz lodes spreading across the NW and SE sectors of the mine, respectively, could be interpreted as a contribution of this latter source superimposed onto the advected mass and the heat flow circuits related to the greisen-granite cupola placed to the NE. In these circumstances, both fluid sources would have acted almost concurrently.

6.1. Time Constraints for the Mineralization Onset and Subsequent Ore Stages

The age estimates provided by the U-Th-Pb composition of uraninite in greisen samples yielded $\approx 298 \pm 2$ Ma for coarser interstitial grains at the interface of primary quartz and secondary white mica and $\approx 283 \pm 2$ Ma for tiny grains included in secondary coarse-grained white mica. These ages differ significantly from each other and from the whole-rock Rb-Sr dating 289 ± 4 Ma indicated for the two-mica granite considered the parental rock of greisen [23]. Nonetheless, the 289 ± 4 Ma age should date the ending of common Rb and Sr diffusion processes coeval with the time when the crystallization path of granite crossed the closure temperature of that isotopic system (≈ 650 °C), assuming that the analyzed samples were not affected by late metasomatic processes strong enough to disturb the measured Rb and Sr abundances. Consequently, the $\approx 298 \pm 2$ Ma age could be interpreted as the best approximation for the timing of granite emplacement. This represents a minimum age because effects of some Pb loss during superimposed transformations experienced by the greisen cupola could not be discarded. Effective Pb removal during late alteration processes in greisen should have affected preferentially tiny uraninite grains within secondary mica, thus explaining the obtained divergent younger age.

The $\approx 298 \pm 2$ Ma minimum age inferred for the granite emplacement is consistent with other published data, namely: (i) 305.2 ± 5.7 Ma, U-Pb in rutile [139] occurring along with tourmaline (*Tour Ia* in this work); (ii) 303 ± 3.3 Ma and 301 ± 4.2 Ma, U-Pb in cassiterite [140] coexisting with topaz (*Tpz Ia* in this work); and (iii) 296.3 ± 0.8 Ma, Ar-Ar in mica [61] forming thick selvages of quartz lodes (*Ms Ia* in this work). Therefore, the multiple fluid influxes related to the onset of ore-forming processes could be placed within the 299 ± 5 Ma time window, as suggested by the joint interpretation of these data (Figure 13). In addition, the Ar-Ar age of late mica in quartz lodes (291.6 ± 0.8 Ma) [61] indicates that the ore forming process at Panasqueira should have protracted for several million years. According to the available information [61], this late mica is equivalent to *Ms II*; therefore, a period of

ca. 5 to 7 Ma is required to embrace all the ore forming events included in the “oxide–silicate” and “main sulfide” evolving stages. This is also the time that separates the growth of *Ms Ia* and *Ms II*, confined to 4.7 ± 1.1 Ma if the Ar-Ar dating is solely considered. Therefore, the late *Ms II* + *Tpz II* + *Apt II* (\pm *Cst II* \pm *Wolf II*) assemblage formed shortly after *Tour II* should show a distinct fluid influx into the lode system, which shows an important (and possibly short-lived) rejuvenation event after the “main sulfide stage”. This event, although recognised in many of the quartz lodes, is particularly well documented in quartz lodes distributed across the E–NE and NW sectors of the mine.

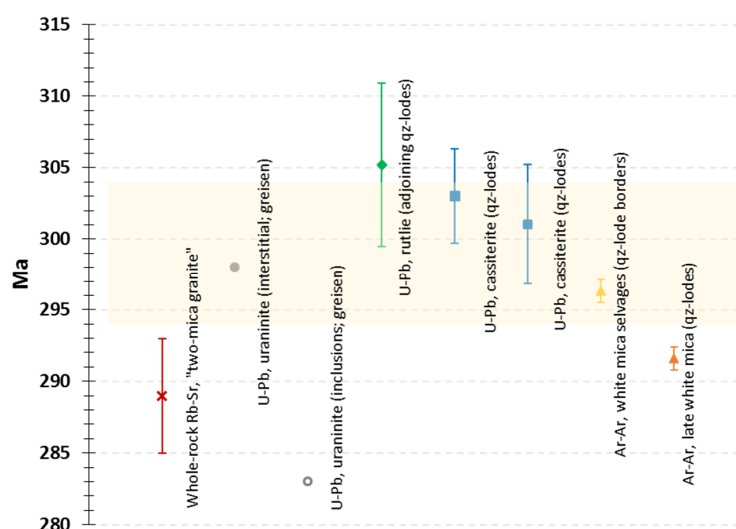


Figure 13. Graphic representation of the ages determined so far for the Panasqueira system, allowing the inference of 299 ± 5 Ma for the multiple fluid influxes related to the onset of ore-forming processes in the Panasqueira system. The (short-lived?) rejuvenation event should have occurred at ca. 292 Ma.

6.2. Chemical Changes in Fluids Indicated by Silicate–Oxide–Phosphate Associations

Variations in mineral composition depend on many factors. However, in geological settings such as those represented by quartz lodes and their margins at Panasqueira, these variations are mostly ruled by mineral–fluid elemental partitioning, which is quite sensitive to P–T conditions and element speciation in fluids [187–190]. Therefore, the obtained compositional variations for silicates, oxides and phosphates can be used to assess some of the main chemical features of fluids involved in each evolving stage of the ore system. In this assessment, however, two additional effects must be considered: the influence of element partitioning between coexisting mineral phases; and the controls imposed by local chemical gradients related to adjustments of wall–rock mineral assemblages or mineral infillings previously deposited in quartz lodes when in contact with chemically reactive fluids. Both effects could be duly appreciated if compositions of concurrent mineral phases were considered jointly to infer fluid characteristics, and if each group or subgroup of analytical data representing a given mineral phase could be assigned to a particular background.

The pre-ore stage (i.e., previous to *Cst I* and *Wolf I* deposition) is basically traced by the growth of rutile + *Tour Ia* \pm monazite in wall rocks of quartz lodes, often accompanied by tourmalinization of variable intensity. As mentioned before, this record is quite well preserved in the northern sectors of the mine, particularly in those close to the known greisen-granite cupola, even though it is recognizable westwards of it. In this mineral assemblage, the cores of rutile grains are enriched in Nb, Ta and V (\pm Fe^{3+} , Zr) in comparison with their rims, which occasionally display higher W contents. Coexisting Na-rich *Tour Ia* also shows variable composition, with cores enriched in Mg (\pm Ca) and borders typically displaying increased abundances of Fe^{2+} (\pm Ti, F, Li); these trends are also evidenced by tourmaline within alteration haloes, wherein occasional *Apt I* was found. This apatite includes significant minor amounts of Fe^{3+} and REE, besides traces of Mn, Sr, Mg, Na and Cl. Therefore,

accepting that metasedimentary rocks could have acted as a preferential source for some elements (such as Al, Mg, Sr, V or even Zr) when reacting with B-rich fluids under low fluid/rock ratios [59,129], the chemical input related to fluid inflows is evident and should have involved a large number of elements other than Na and Fe. These chemical fingerprints became more intense as fluid/rock ratios increased and thick *Ms Ia* selvages formed.

Micas in thick selvages are F-rich and their Fe contents usually higher than Mg; sodium is always a significant minor constituent. During the early steps of *Ms Ia* growth, Sn is incorporated in trace amounts along with other elements (Ti, Ba, Ca, Mn), and the Fe-rich rims of coexisting *Tour Ia* tend to present more consistent and higher trace amounts of F and Li, occasionally coupled with Zn. The *Ms Ia* rims, recording the late growing steps of coarse-grained mica plates that in many samples is concurrent of *Cst I* formation, do not incorporate Sn and are clearly enriched in Li, partially replacing Al in octahedral sites. To the west of the greisen-granite cupola and in contrast with *Tour Ia* or the corroded irregular grains of *Apt I*, the composition of *Ms Ia* changes as the selvages became gradually enriched in topaz and cassiterite. In these settings, mica is almost devoid of Mg and a significant part of the iron is ferric; F and Na remain high, but trace amounts of Ti are much more irregular and Sn is always below the EPMA detection limit. The fringes of this *Ms Ia* mica are also enriched in Li, although preferentially occupying the octahedral vacancies.

Quartz lodes in the SW sector of the mine are typically bordered by thick *Tpz Ia* selvages variably enriched in *Cst I*, along with accessory rutile, *Tour Ia* and corroded *Apt I*. In these settings, rutile grains display relative uniform compositions, usually comparable to those presented by the rims of rutile in tourmaline-rich assemblages, although bearing slightly higher Zr concentrations. Remnants of *Apt I* maintain meaningful Fe^{3+} and REE abundances. Tourmaline preserves the main compositional features of *Tour Ia* in mica selvages, despite the tendency to display thicker Fe-rich borders with consistently higher F contents. Topaz is quite homogeneous in composition and shows significant Fe^{3+} and REE (\pm Zn) concentrations, not differing significantly from *Tpz Ia* occurrences in mica selvages but preserving distinctive inclusions of gorceixite-like phosphates. Relevant abundances of Fe^{3+} and V (\pm Ti, W, Zn) characterize coexistent *Cst I* grains, which also comprise very similar phosphate inclusions, thus documenting a common fingerprint developed before the prevailing influx of the F-rich fluid into the system.

The thin and frequently discontinuous bands that decorate quartz lodes placed to the SSW of the greisen-granite cupola comprise *Ms Ib*, sometimes along with accessory *Tour Ib* and *Tpz Ib*. This F-rich mica is compositionally similar to core–border transitions and rims of *Ms Ia* in thick selvages nearby the cupola; Sn concentrations always remain below the EPMA detection limit, but trace amounts of Cs emerge as a distinctive feature. The composition of *Tour Ib* is characterized by relatively high abundances of Fe^{2+} and Na (\pm F, Li), and coexisting *Tpz Ib* includes Fe^{3+} , Zn and Ba. Therefore, the composition of fluid influxes related to this mineral assemblage was not exactly the same as that involved in the development of thick selvages comprising *Ms Ia* or *Tpz Ia* observed in the northern and southwestern sectors of the mine. Several chemical characteristics are shared, but differences in B, F and P (\pm Sn, Na, Cs) availability are noteworthy. In this regard, it should be noted that the composition of *Ms Ib* in lode borders is comparable to mica infillings of fractures criss-crossing *Ms Ia* thick selvages, despite the lower abundances of Li in the latter (preferentially occupying octahedral vacancies).

The composition of *Wolf I* is rather homogeneous, documenting an evident availability of Fe in relation to Mn. Relative enrichments in Zr (\pm Ti) and Nb (\pm Ta) are also significant in many core domains of *Wolf I*, although not defining any regular trend. In quartz lodes with thick mica selvages, *Wolf I* deposition occurred mostly after the late steps of *Ms Ia* growth and preceded, at least in part, *Ms Ib* in fracture infillings. The formation of this oxide also took place after *Cst I* was included in either *Ms Ia*- or *Tpz Ia*-rich selvages. Thus, the composition of fluids to which *Wolf I* is conceivably related should approximate that inferred for fluid inflows implicated in the initial evolving steps of quartz lodes with discontinuous thin bands of *Ms Ib*. This explains why tungsten-rich lodes are not necessarily bordered by mica selvages (locally, these may even be absent), although the frequent preservation

of tiny isokite- or isoclasite-like phosphate inclusions in *Wolf I* may be used as evidence for an early (and incipient) inflow of fluids providing P, Ca, Fe and F (\pm Na, Mg), as in other parts of the lode system.

Deposition of *Tour Ic* and *Ms Ic* post-dates *Wolf I* and documents episodic inflows of (Fe, Na, F \pm Ba)-bearing fluids into quartz lodes locally affected by fracture networks of limited extension. Subsequent irregular fluid influxes reacting with previously deposited *Ms Ic* and *Wolf I* allowed the growth of the Fe-rich *Chl I* (sometimes incorporating Mn, besides trace amounts of F and Zn), which outlines the waning steps of the main “oxide–silicate ore stage”.

Contrary to what is indicated in classical studies on Panasqueira, the observations reported in this work suggest that a (short-lived?) rejuvenation event should have occurred after the “main sulfide stage”, but preceding the “post-ore carbonate stage”. The onset of this event is outlined by the development of *Ms II* + *Tpz II* + *Apt II* (\pm *Cst II* \pm *Wolf II*) assemblage, formed shortly after *Tour II*. In comparison with early tourmalines, *Tour II* is somewhat enriched in Mg, Ca and Li. The composition of *Ms II* is also distinct from previous mica generations, showing higher F and Mg contents, occasionally bearing Li, which tends to replace Al in octahedral positions. Relevant minor amounts of Nb and Ta, besides Fe³⁺ and Ce, characterize *Tpz II*. In *Apt II*, the minor constituents Mn, Fe and Sr occur with meaningful trace amounts of some LREE, Mg, Na and Cl, complementing the chemical fingerprints provided by the occurrence of graptone phosphate in addition to goyazite (most often along with *Tpz II*). The composition of *Cst II* differs from that documented for *Cst I*, revealing distinctive trace amounts of Ta, together with erratic Nb, Cu, Ni and Co contents. On the contrary, *Wolf II* does not display notable differences in composition when compared to *Wolf I* as far as the EPMA can detect. Together these results indicate that fluids driven to quartz lodes in this event should have provided a revitalization of the ore system, renewing the availability of a large number of chemical constituents that are not present during the previous deposition of sulfides. This chemical renewal comprised B, F, P and W (\pm Ta, Nb, REE, Sr, Mn, Na, Li), besides Fe and Sn.

In summary, B-rich fluids carrying significant F (\pm P), Fe and Na (\pm REE, Sn), and gradually enriched in Li, should have prevailed during the mineralization onset in the vicinity of the greisen-granite cupola and immediately to the S–SW of it. The beginning of ore forming processes in the SE sector of the mine was possibly deferred to a later time, and the composition of coeval fluid influxes similar to that involved in the northern mine sectors, although bearing: lower B, F and P (\pm Sn, Ca, Na) abundances; comparable Fe and Li contents; and higher Cs concentrations. Furthermore, their saturation in W (\pm Nb, Ta) occurred quickly. Early mineralization stages in the SW sector of the mine should have mostly involved inflows of F-rich fluids variably enriched in P (\pm B), Fe, Na and Sn (\pm REE, W, Ba). Prevalent redox conditions should have mostly remained below the Fe oxidation threshold, although intermittently achieving values at the Fe²⁺–Fe³⁺ boundary. After *Cst I* and *Wolf I* deposition, episodic inflows of (Fe, Na, F \pm Ba)-bearing fluids are indicated by the growth of *Tour Ic* and *Ms Ic*. However, a significant revitalization of the ore system took place after the “main sulfide” ore stage, particularly affecting the quartz lodes distributed across the E–NE and NW sectors of the mine and accounting for variable inputs in B, F, P, Sn and W (\pm Ta, Nb, REE, Sr, Mn, Na, Li).

6.3. Evolution of Temperature Conditions

Experimental results show that Zr concentrations in rutile vary with temperature (T) [191,192]. Using the log-linear dependence between Zr abundances (ppm) with T⁻¹ (K) and the reviewed calibrations for the Zr-in-rutile thermometer [193], a temperature range from \approx 540 to 590 °C is obtained for $0.5 \leq a\text{SiO}_2 \leq 1.0$ and Zr = 148 ppm, corresponding to the 0.02 wt % median ZrO₂ concentration value characterizing the entire analytical dataset. For the few rutile grains within tourmaline-rich mineral assemblages where independent analyses of cores (\bar{x} = 237 ppm Zr) and rims (\bar{x} = 200 ppm Zr) were possible, temperature values vary from \approx 570 to 625 °C and from \approx 555 to 610 °C, respectively, keeping the same $a\text{SiO}_2$ range. Following the same procedure, temperature estimation for rutile in thick cassiterite-bearing *Tpz I* selvages (\bar{x} = 296 ppm Zr) confines the growth of that oxide to \approx 585–640 °C.

Temperature estimates for rutile formation could also be used to indirectly verify the reliability of compositions displayed by coexistent *Tour Ia*. The analytical data gathered for tourmaline are not thorough enough to use thermometers based on intersectoral element partitioning [194]. However, considering the inverse relationship of $(\text{Na} + \text{Mg} + \text{Fe} - \text{Al})$ contents per formula unit with temperature [194] and the 625–555 °C range obtained for rutile, the resultant $(\text{Na} + \text{Mg} + \text{Fe} - \text{Al})$ values are clearly consistent with those measured for *Tour Ia*. Furthermore, the whole variation obtained for $(\text{Na} + \text{Mg} + \text{Fe} - \text{Al})$ contents in *Tour Ia*, ranging from -3.628 to -2.380 ($\bar{x} = -2.969$), suggests that the growth of tourmaline could have occurred at temperature conditions of the order of 475–500 °C.

The F-OH exchange thermometer assumes an ideal mixing model between muscovite and topaz [195,196]. Thus, estimated temperature values are influenced by the total of R^{2+} ions occupying octahedral sites in muscovite, and for this reason only analyses with $(\sum \text{R}^{2+})^{vi} < 0.4$ were considered [196], which considerably reduced the number of *Ms-Tpz* pairs usable in this approach. Even so, a reasonable set of temperature results were obtained for the *Tpz Ia–Ms Ia*, *Tpz Ib–Ms Ib* and *Tpz II–Ms II* pairs, assuming a pressure range of 20 to 200 MPa (Figure 14). According to these results, early phases of quartz lode development should have proceeded under temperature conditions of 474–468 °C (median values for *Ms Ia–Tpz Ia* pair). Subsequent phases of mineral deposition after *Wolf I* should have progressed under temperature conditions of 397–393 °C (median values for *Ms Ib–Tpz Ib* pair). The early phases of the rejuvenation event following the “main sulfide stage” should have occurred under temperature conditions of 447–442 °C (median values for *Ms II–Tpz II* pair).

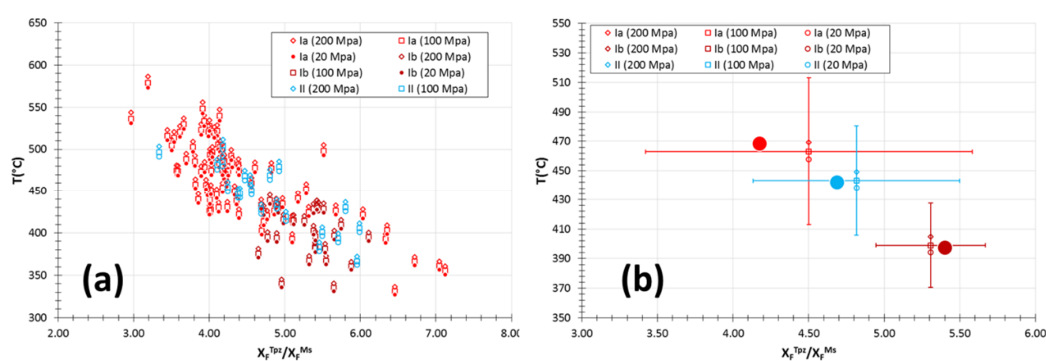


Figure 14. (a) Temperature estimates based on the F-OH exchange thermometer, assuming an ideal mixing model between muscovite and topaz and $20 \leq p \leq 200$ MPa [196]. (b) Mean (and standard error bars) and median temperature values for the *Tpz Ia–Ms Ia*, *Tpz Ib–Ms Ib* and *Tpz II–Ms II* pairs.

Compositional variations of chlorite are quite sensitive to temperature conditions and local chemical gradients, and several empirical and thermodynamic-based thermometric approaches have been developed to date [197–203]. The obtained compositions for *Chl I*, *Chl II* and *Chl III* are suitably described by several ion exchange mechanisms that also constitute the mainstay of some solid-solution models. The selected approach [202], using six endmember components and assuming an ideal mixing on sites with ordered cationic distribution, shows that temperature conditions of chlorite formation vary significantly (Figure 15). Despite some data scattering, mostly in subgroups 1 and 2 of *Chl I*, the range of temperature values is small in comparison with the high variation of $\text{Fe}/(\text{Fe} + \text{Mg})$ ratios shown by each chlorite generation. Therefore, according to these results, subgroups 1 and 2 of *Chl I* were formed at median temperatures of ≈ 350 °C and ≈ 320 °C, respectively, which should represent the prevalent T-conditions during the fading of the “oxide–silicate stage”. Subgroups 1 and 2 of *Chl II*, developed at the transition to the carbonate post-ore evolving stage, display median formation temperatures of ≈ 250 and ≈ 270 °C, respectively. The growth of chlorite related to late, fault-controlled hydrothermal activity (subgroups 1 and 2 of *Chl III*) occurred under T-conditions ranging from ≈ 230 to ≈ 225 °C.

The chart in Figure 16 illustrates the temperature variation in time, from the mineralization onset to its fading, throughout the main ore-forming stages. Temperature conditions inferred for the late growth of *Tour Ia* and assessed with F-OH exchange between *Ms Ia* and *Tpz Ia* (≈ 470 – 500 °C) are

consistent with values estimated in other studies [129] using Ti-in-quartz thermometry (549–420 °C, 100 MPa; 530–404 °C, 20 MPa). These estimations are also comparable with results yielded by B isotope muscovite-tourmaline thermometry in lode selvages, clustering within the 400–460 °C range [131], and the 498 ± 46 °C indicated for arsenopyrite disseminations in thick *Ms Ia* selvages coexisting with *Cst I* [121,204]. Deposition of *Ms Ib* and *Topz Ib* at ≈ 390 –400 °C should trace the ending of *Wolf I* formation in the “oxide–silicate stage”, which further progressed until the growth of *Chl I* at ≈ 350 –320 °C. Therefore, the “oxide–silicate stage” is mostly confined to temperature conditions ranging from ≈ 500 to ≈ 320 °C, being preceded by significant development of rutile and *Tour Ia* under higher temperatures (≈ 640 to ≈ 540 °C, depending on $a\text{SiO}_2$).

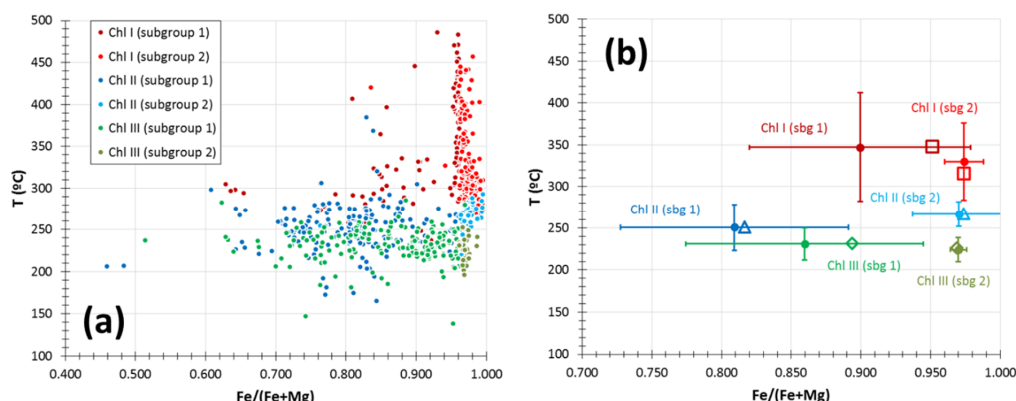


Figure 15. (a) Fe/(Fe + Mg) ratios vs. temperature estimates for chlorite formation based on the six endmember components model that assumes an ideal mixing on sites with ordered cationic distribution [204]. (b) Mean (and standard error bars) and median temperature values for each subgroup of analyses representing the three chlorite generations identified.

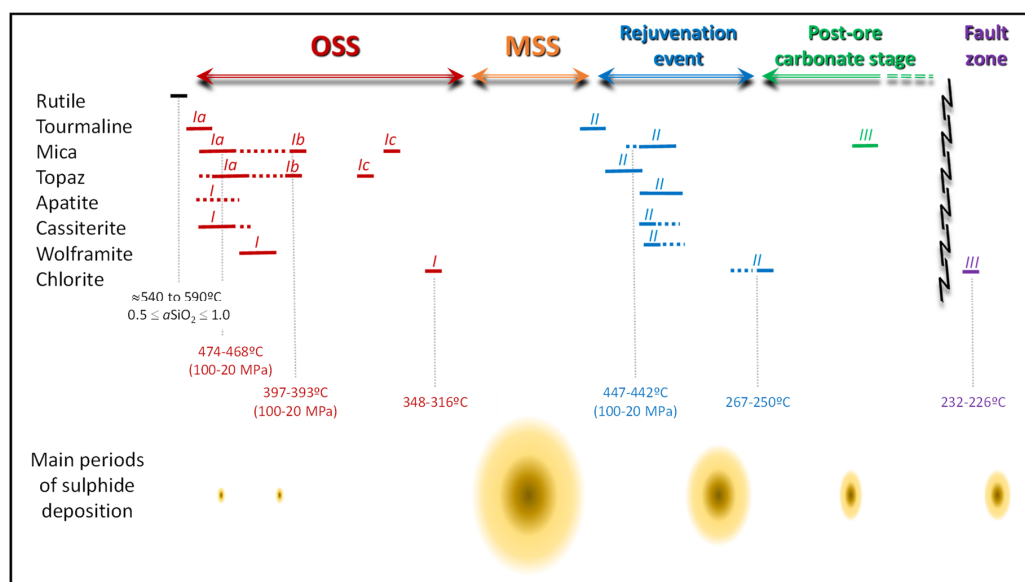


Figure 16. Synoptic outline of temperature conditions and relative position of the main silicates (tourmaline, white mica, topaz and chlorite), oxides (rutile, cassiterite and wolframite) and phosphates (mostly apatite) examined in this work. Sulfide deposition is indicated for general reference and the size of each ellipse intends to qualitatively inform readers about the amount of sulfides formed in each period. Note that the length of double-angled lines representing the main evolving stages of the ore system merely reflects a graphic configuration shaped by the information discussed in the text and is not proportional to the time interval that should be assigned to the pre-ore stage, oxide–silicate stage (OSS), main sulfide stage (MSS), rejuvenation event or post-ore carbonate stage. The same is true for mineral infillings of fault zones.

Temperature conditions for the “main sulfide stage” are poorly constrained by mineral thermometry data. Even so, estimations based on sulfide equilibria and also considering the compositions of arsenopyrite and pyrrhotite deposited during this second ore stage [121,204] point to temperature values of 468 ± 8 and 406 ± 3 °C, respectively. Therefore, the “oxide–silicate stage” to “main sulfide stage” transition should have implicated the inflow of hotter and compositionally different fluids into quartz lodes, culminating with the formation of *Tour II*.

A new (short-lived?) rejuvenation event took place after the “main sulfide stage”, as indicated by *Ms II + Tpz II + Apt II* (\pm *Cst II* \pm *Wolf II*) formation, followed by some sulfides (including molybdenite) [127]. Temperature conditions for the onset of this event are provided by the *Ms II–Tpz II* pair (\approx 440–450 °C), which are consistent with the growth of a late arsenopyrite at 437 ± 27 °C [121,204], both preceding *Chl II* (\approx 250–270 °C) and the progression towards the final carbonate post-ore evolution stage.

In conclusion, the swarm of quartz lodes at Panasqueira show a series of opening and closing events extending for several million years and involving multiple fluid influxes of variable composition. The reconstructed temperature–time path based on mineral thermometry is much wider than that inferred on the basis of published fluid inclusion data, which indicate low to moderate ($< \approx 360$ °C) temperature conditions for the main ore stages [58,113,143,144,149,151]. This discrepancy reflects the difficulty in gathering microthermometry data representative of all phases of mineral deposition in lodes, along with the poor preservation of primary fluid inclusions in some mineral generations (such as quartz) due to their intense deformation.

7. Conclusions

Mineral infillings of the Panasqueira lodes are diverse and not evenly recorded in all of the mine sectors. Four different geological trends can be observed on the basis of mineral assemblages forming the lode borders and the relative abundances of wolframite and cassiterite. These geological trends show important disparities for the onset of mineralization in sectors nearby or far from the known greisen-granite cupola, reflecting the involvement of multiple fluid influxes with somewhat distinct compositions. In general, the ore-forming process progressed from an early “oxide–silicate stage” (OSS) to a “main sulfide stage” (MSS), and further on to a post-ore carbonate stage. However, according to the reported observations and interpretations, an important (short-lived?) rejuvenation event should have occurred after MSS. The present study is confined to mineral associations comprising silicates (tourmaline, white mica, topaz and chlorite), oxides (rutile, cassiterite, wolframite) and phosphates (mostly apatite), and so inferences on fluid composition and temperature conditions are limited to the OSS and the waning steps of MSS, followed by the rejuvenation event.

Adjoining the greisen-granite cupola and immediately to the S–SW of it, the lodes are mainly bordered by thick *Ms Ia* selvages comprising *Tour Ia* (\pm *Apt I*), and *Wolf I* prevails over *Cst I*. To the west of the cupola, *Ms Ia* selvages of considerable thickness also form the edges of the most characteristic lodes, but they are gradually enriched in *Tpz Ia* and *Cst I* as the distance to the cupola increases, which is roughly coupled by a gradual decreasing in *Tour Ia* and *Wolf I*. In these mine sectors, the pre-ore stage (previous to *Cst I* and *Wolf I* deposition) comprises the growth of rutile + *Tour Ia* \pm monazite in wall rocks of quartz lodes, often accompanied by tourmalinization of variable intensity. The prevailing inflow of B-rich fluids into the fractured rock mass should have also carried significant amounts of F (\pm P), Fe and Na (\pm REE, Sn), becoming gradually enriched in Li. After *Cst I* and *Wolf I* deposition, episodic inflows of (Fe, Na, F \pm Ba)-bearing fluids are documented by the growth of *Tour Ic* and *Ms Ic*.

Further SSW, far from the known cupola, the most common lode borders are outlined by thin (often discontinuous) bands of *Ms Ib* (\pm *Tour Ib* and *Tpz Ib*), and *Wolf I* occurs along with accessory *Cst I* whenever present. The beginning of ore-forming processes in this mine sector was possibly deferred in time, and the composition of coeval fluid influxes is similar to those involved in the northern mine sectors, although bearing: lower B, F and P (\pm Sn, Ca, Na) abundances; comparable Fe and Li contents; and higher Cs concentrations. Their saturation in W (\pm Nb, Ta) should have occurred quickly.

In the SW sector of the mine, the lodes are typically bordered by thick *Tpz Ia* selvages comprising rutile and several phosphates, and *Cst I* largely predominates over *Wolf I*. The early mineralization stages should have involved mostly inflows of F-rich fluids variably enriched in P (\pm B), Fe, Na and Sn (\pm REE, W, Ba). This opens the possibility of a second source of mineralizing fluids existing to the SW, linked with an outgrowth of the batholith to which the known cupola also belongs or related to a distinct granite body.

The multiple fluid influxes related to the onset of ore-forming processes could be placed within the 299 ± 5 Ma time window. Using the median value of ZrO₂ concentrations in rutile, temperature estimations provided by the Zr-in-rutile thermometer range from ≈ 640 to ≈ 540 °C, depending on the *a*SiO₂. Temperatures inferred for *Tour Ia* late growth and assessed with the F-OH exchange between *Ms Ia* and *Tpz Ia* vary between ≈ 470 and 500 °C. Deposition of *Ms Ib* and *Tpz Ib* at ≈ 390 –400 °C should trace the waning steps of *Wolf I* formation in OSS, which further progressed until *Chl I* growth at ≈ 350 –320 °C. The (short-lived?) rejuvenation event occurred at ca. 292 Ma and is quite well documented in quartz lodes distributed across the E–NE and NW sectors of the mine. This event is indicated by the mineral assemblage *Ms II + Tpz II + Apt II* (\pm *Cst II* \pm *Wolf II*), formed shortly after *Tour II* and followed by some sulfides (including molybdenite). It documents a distinct fluid influx into the lode system that allowed a renewal of B, F, P, Sn and W (\pm Ta, Nb, REE, Sr, Mn, Na, Li) inputs. Temperature conditions for the onset of this event are provided by the *Ms II*–*Tpz II* pair (≈ 440 –450 °C), preceding *Chl II* (≈ 250 –270 °C) and the progression towards the final carbonate post-ore evolution stage.

Supplementary Materials: The following are available online at <http://www.mdpi.com/2075-163X/10/6/551/s1>: Table S1: EPMA analytical profiles used for assess the compositional characteristics of silicates, phosphates and oxides. Table S2: Representative analyses, ion distributions per formula unit and range of concentrations (in wt %) of essential elements in tourmaline. Table S3: Representative analyses, ion distributions per formula unit and range of concentrations (in wt %) of essential elements in mica. Table S4: Representative analyses, ion distributions per formula unit and range of concentrations (in wt %) of essential elements in topaz. Table S5: Representative analyses, ion distributions per formula unit and range of concentrations (in wt %) of essential elements in chlorite. Table S6: Representative analyses, ion distributions per formula unit and range of concentrations (in wt %) of essential elements in rutile. Table S7: Representative analyses, ion distributions per formula unit and range of concentrations (in wt %) of essential elements in cassiterite. Table S8: Representative analyses, ion distributions per formula unit and range of concentrations (in wt %) of essential elements in wolframite. Table S9: Uraninite analyses in greisen samples. Table S10: Representative analyses, ion distributions per formula unit and range of concentrations (in wt %) of essential elements in apatite. Figure S1: Compositional variation of the analyzed topaz resulting from Al³⁺ substitution by R²⁺ or R⁵⁺. Figure S2: Compositional variation of the analyzed rutile considering the relative abundance of prevalent minor constituents and their roles in the general exchange mechanism involved in Ti substitution. Figure S3: Cross-plots illustrating the substitution of Sn in cassiterite. Figure S4: Scatter plots documenting the main ion substitution mechanisms involved in wolframite, besides the usual Fe²⁺ = Mn²⁺ interchange. Figure S5: Examples of interstitial uraninite at the interface of primary quartz and secondary white mica, and as inclusions in secondary coarse-grained white mica.

Author Contributions: A.M., conceptualization, petrography, numerical handling of analytical data, mineral thermometry, data interpretation, writing (original draft preparation, review and editing), and funding acquisition. J.F., numerical handling of analytical data, data interpretation, writing (review and editing) and funding acquisition. I.M., sampling and sample preparation, petrography, EPMA work, data interpretation and writing (review and editing). P.C.R., conceptualization, test and validation of analytical profiles with EPMA, data accomplishment and subsequent processing, writing (review and editing). F.P., conceptualization and completion of the sampling program, writing (review and editing). All authors have read and agreed to the published version of the manuscript.

Funding: This study, developed under the scope of the ERA-MIN joint call project “NewOreS”, was financially supported by the Portuguese funding agency for Science, Research and Technology (FCT). Additional backing was obtained from the projects FCT/UID/GEO/50019/2019 and UIDB/50019/2020 (IDL).

Acknowledgments: The authors are most grateful to Beralit Tin and Wolfram S.A. for permitting access to the Panasqueira Mine and for the support provided to Ivo Martins. The administrative support of Célia Lee is also warmly acknowledged. Constructive comments by three anonymous reviewers were much appreciated.

Conflicts of Interest: The authors declare no conflicts of competing financial interests or personal relationships that could have influenced the work reported in this paper.

References

1. Linnen, R.L.; Van Lichtervelde, M.; Černý, P. Granitic pegmatites as sources of strategic metals. *Elements* **2012**, *8*, 275–280. [[CrossRef](#)]
2. Gunn, G. *Critical Metals Handbook*; John Wiley & Sons, Ltd.: Hoboken, NJ, USA, 2013.
3. Dehainea, Q.; Filippova, L.O.; Glass, H.J.; Rollinson, G. Rare-metal granites as a potential source of critical metals: A geometallurgical case study. *Ore Geol. Rev.* **2019**, *104*, 384–402. [[CrossRef](#)]
4. Černý, P.; Blevin, P.L.; Cuney, M.; London, D. Granite-related ore deposits. In *Economic Geology*; Hedenquist, J.W., Thompson, J.F.H., Goldfarb, R.J., Richards, J.R., Eds.; Society of Economic Geologists, Inc.: Littleton, CO, USA, 2005; Volume 100th Anniversary, pp. 337–370.
5. Duchoslav, M.; Marks, M.A.W.; Drost, K.; McCammon, C.; Marschall, H.R.; Wenzel, T.; Markl, G. Changes in tourmaline composition during magmatic and hydrothermal processes leading to tin-ore deposition: The Cornubian Batholith, SW England. *Ore Geol. Rev.* **2017**, *83*, 215–234. [[CrossRef](#)]
6. Wang, R.C.; Xie, L.; Chen, J.; Yu, A.; Wang, L.; Lu, J.; Zhu, J. Tin-carrier minerals in metaluminous granites of the western Nanling Range (southern China): Constraints on processes of tin mineralization in oxidized granites. *J. Asian Earth Sci.* **2013**, *74*, 361–372. [[CrossRef](#)]
7. Simons, B.; Andersen, J.C.Ø.; Shail, R.K.; Jenner, F.E. Fractionation of Li, Be, Ga, Nb, Ta, In, Sn, Sb, W and Bi in the peraluminous Early Permian Variscan granites of the Cornubian Batholith: Precursor processes to magmatic-hydrothermal mineralization. *Lithos* **2017**, *278*, 491–512. [[CrossRef](#)]
8. Harlaux, M.; Mercadier, J.; Marignac, C.; Peiffert, C.; Cloquet, C.; Cuney, M. Tracing metal sources in peribatholithic hydrothermal W deposits based on the chemical composition of wolframite: The example of the Variscan French Massif Central. *Chem. Geol.* **2018**, *479*, 58–85. [[CrossRef](#)]
9. Schmidt, C. Formation of hydrothermal tin deposits: Raman spectroscopic evidence for an important role of aqueous Sn(IV) species. *Geochim. Cosmochim. Acta* **2018**, *220*, 499–511. [[CrossRef](#)]
10. Schmidt, C.; Romer, R.L.; Wohlgemuth-Ueberwasser, C.C.; Appelt, O. Partitioning of Sn and W between granitic melt and aqueous fluid. *Ore Geol. Rev.* **2020**, *117*, 103263. [[CrossRef](#)]
11. Liu, X.; Xiao, C. Wolframite solubility and precipitation in hydrothermal fluids: Insight from thermodynamic modeling. *Ore Geol. Rev.* **2020**, *117*, 103289. [[CrossRef](#)]
12. Schuiling, R.D. Tin belts on the continents around the Atlantic Ocean. *Econ. Geol.* **1967**, *62*, 540–550. [[CrossRef](#)]
13. Routhier, P. A new approach to metallogenic provinces; the example of Europe. *Econ. Geol.* **1976**, *71*, 803–811. [[CrossRef](#)]
14. Derré, C. Caractéristiques de la distribution des gisements à étain et tungstène dans l’ouest de l’Europe. *Miner. Deposita* **1982**, *17*, 55–77. [[CrossRef](#)]
15. Marignac, C.; Cuney, M. Ore deposits of the French Massif Central: Insight into the metallogenesis of the Variscan collision belt. *Miner. Deposita* **1999**, *34*, 472–504. [[CrossRef](#)]
16. Blundell, D.; Arndt, N.; Cobbold, P.R.; Heinrich, C. Geodynamics and ore deposit evolution in Europe. *Ore Geol. Rev.* **2005**, *27*, 345. [[CrossRef](#)]
17. De Vos, W.; Batista, M.J.; Demetriades, A.; Duris, M.; Lexa, J.; Lis, J.; Marsina, K.; O’Connor, P.J. Metallogenic mineral provinces and world class ore deposits in Europe. In *IUSGS/ILAGC Global Geochemical Baselines*; EuroGeoSurveys: Brussels, Belgium, 2005.
18. Kerrich, R.; Goldfarb, R.J.; Richards, J.P. Metallogenic provinces in an evolving geodynamic framework. In *Economic Geology*; Hedenquist, J.W., Thompson, J.F.H., Goldfarb, R.J., Richards, J.R., Eds.; Society of Economic Geologists, Inc.: Littleton, CO, USA, 2005; Volume 100th Anniversary, pp. 1097–1136.
19. Bouchot, V.; Ledru, P.; Lerouge, C.; Lescuyer, J.-L.; Milesi, J.-P. Late Variscan mineralizing systems related to orogenic processes: The French Massif Central. *Ore Geol. Rev.* **2005**, *27*, 169–197. [[CrossRef](#)]
20. Romer, R.L.; Thomas, R.; Stein, H.J.; Rhede, D. Dating multiply overprinted Sn-mineralized granites—examples from the Erzgebirge, Germany. *Miner. Deposita* **2007**, *42*, 337–359. [[CrossRef](#)]
21. Harlaux, M.; Romer, R.L.; Mercadier, J.; Morloti, C.; Marignac, C.; Cuney, M. 40 Ma of hydrothermal W mineralization during the Variscan orogenic evolution of the French Massif Central revealed by U-Pb dating of wolframite. *Miner. Deposita* **2018**, *53*, 21–51. [[CrossRef](#)]
22. Gourcerol, B.; Gloaguen, E.; Melleton, J.; Tudur, J.; Galiegue, X. Re-assessing the European lithium resource potential—A review of hard-rock resources and metallogeny. *Ore Geol. Rev.* **2019**, *109*, 494–519. [[CrossRef](#)]

23. Priem, D.; Tex, T. Tracing crustal evolution in the NW Iberian Peninsula through the Rb-Sr and U-Pb systematics of Paleozoic granitoids: A review. *Phys. Earth Planet. Interiors* **1984**, *35*, 121–130. [[CrossRef](#)]
24. Ferreira, N.; Iglesias, M.; Noronha, F.; Pereira, E.; Ribeiro, A.; Ribeiro, M.L. Granitóides da Zona Centro Ibérica e seu enquadramento geodinâmico. In *Geologia de Los Granitoides y Rocas Asociadas del Macizo Hespérico Libro Homenaje a LC Garcia de Figuerola*; Bea, F., Carnicero, E., Gonzalo, J.C., Plaza, M.L., Rodríguez, M.D., Eds.; Rueda: Madrid, Spain, 1987; pp. 37–53.
25. Reavy, R.J. Structural controls on metamorphism and syn-tectonic magmatism: The Portuguese hercynian collision belt. *J. Geol. Soc. Lond.* **1987**, *146*, 649–657. [[CrossRef](#)]
26. Reavy, R.J.; Stephens, W.E.; Fallick, A.E.; Halliday, A.N.; Godinho, M.M. Geochemical and isotopic constraints on petrogenesis: The Serra da Freita pluton, a typical granite body from the Portuguese Hercynian collision belt. *Geol. Soc. Am. Bull.* **1991**, *193*, 392–401. [[CrossRef](#)]
27. Vignerresse, J.L. Intrusion level of granitic massifs along the Hercynian belt: Balancing the eroded crust. *Tectonophysics* **1999**, *307*, 277–295. [[CrossRef](#)]
28. Henk, A.; von Blackenburg, F.; Finger, F.; Schaltegger, U.; Zulauf, G. Syn-convergent high-temperature metamorphism and magmatism in the Variscides: A discussion of potential heat sources. In *Orogenic Processes: Quantification and modelling, Variscan Belt* (W. Frank, V. Haak, O. Oncken, D. Tanner, Eds.). *Geol. Soc. Lond. Spec. Publ.* **2000**, *179*, 387–399. [[CrossRef](#)]
29. Fernandez-Suarez, J.; Dunning, G.R.; Jenner, G.A.; Gutierrez-Alonso, G. Variscan collisional magmatism and deformation in NW Iberia: Constraints from U-Pb geochronology of granitoids. *J. Geol. Soc. Lond.* **2000**, *157*, 565–576. [[CrossRef](#)]
30. Dias, G.T. Fontes de granitóides hercínicos da Zona Centro-Ibérica (Norte de Portugal): Evidências isotópicas (Sr, Nd). In *Geoquímica e Petrogênese de Rochas Granitóides*; Neiva, A.M.R., Ed.; Mem. Acad. Ciên.; Academia das Ciências de Lisboa: Lisboa, Portugal, 2001; pp. 21–43.
31. Ribeiro, M.L. Modelos de implantação dos granitos variscos portugueses. In *Geoquímica e Petrogênese de Rochas Granitóides*; Neiva, A.M.R., Ed.; Mem. Acad. Ciên.; Academia das Ciências de Lisboa: Lisboa, Portugal, 2001; pp. 33–52.
32. Bea, F.; Montero, P.; Zinger, T. The nature, origin and thermal influence of the granite source layer of Central Iberia. *J. Geol.* **2003**, *111*, 579–595. [[CrossRef](#)]
33. Valle Aguado, B.; Azevedo, M.R.; Schaltegger, U.; Martínez-Catalán, J.R.; Nolan, J. U/Pb zircon and monazite geochronology of Variscan magmatism related to synconvergence extension in Central Northern Portugal. *Lithos* **2005**, *82*, 169–184. [[CrossRef](#)]
34. Fernández-Suarez, J.; Gutierrez-Alonso, G.; Johnston, S.T.; Jeffries, T.E.; Pastor-Galán, D.; Jenner, G.A.; Murphy, J.B. Iberian late-Variscan granitoids: Some considerations on crustal sources and the significance of “mantle extraction ages”. *Lithos* **2011**, *123*, 121–132. [[CrossRef](#)]
35. Manning, D.A.C.; Pichavant, M. The role of fluorine and boron in the generation of granitic melts. In *Migmatites, Melting and Metamorphism*; Atherton, M.P., Gribble, C.D., Eds.; Shiva Publishing Unlimited: Nantwich, UK, 1983; pp. 94–109.
36. Tischendorf, G.; Förster, H.-J. Acid magmatism and related metallogensis in the Erzgebirge. *Geol. J.* **1990**, *25*, 443–454. [[CrossRef](#)]
37. Bea, F.; Fershtater, G.; Corretgé, L.G. The geochemistry of phosphorus in granite rocks and the effect of aluminium. *Lithos* **1992**, *29*, 43–56. [[CrossRef](#)]
38. Bea, F.; Pereira, M.D.; Stroh, A. Mineral/leucosome trace-element partitioning in a peraluminous migmatite (a laser ablation-ICP-MS study). *Chem. Geol.* **1994**, *117*, 291–312. [[CrossRef](#)]
39. Brown, M.; Rushmer, T. *Evolution and Differentiation of the Continental Crust*; Cambridge University Press: Cambridge, UK, 2006.
40. Romer, R.L.; Förster, H.-J.; Hahne, K. Strontium isotopes—A persistent tracer for the recycling of Gondwana crust in the Variscan orogen. *Gondwana Res.* **2012**, *22*, 262–278. [[CrossRef](#)]
41. Romer, R.L.; Meixner, A.; Förster, H.-J. Lithium and boron in late-orogenic granites—Isotopic fingerprints for the source of crustal melts? *Geochim. Cosmochim. Acta* **2014**, *131*, 98–114. [[CrossRef](#)]
42. Romer, R.L.; Meixner, A.; Hahne, K. Lithium and boron isotopic composition of sedimentary rocks—The role of source history and depositional environment: A 250 Ma record from the Cadomian orogeny to the Variscan orogeny. *Gondwana Res.* **2012**, *26*, 1093–1110. [[CrossRef](#)]

43. Romer, R.L.; Kroner, U. Sediment and weathering control on the distribution of Paleozoic magmatic tin–tungsten mineralization. *Miner. Deposita* **2015**, *50*, 327–338. [[CrossRef](#)]
44. Romer, R.L.; Kroner, U. Phanerozoic tin and tungsten mineralization—Tectonic controls on the distribution of enriched protoliths and heat sources for crustal melting. *Gondwana Res.* **2016**, *31*, 60–95. [[CrossRef](#)]
45. Wolf, M.; Romer, R.L.; Franz, L.; López-Moro, F.J. Tin in granitic melts: The role of melting temperature and protolith composition. *Lithos* **2018**, *310*, 20–30. [[CrossRef](#)]
46. Tichomirowa, M.; Gerdes, A.; Lapp, M.; Leonhardt, D.; Whitehouse, M. The chemical evolution from older (323–318 Ma) towards younger highly evolved tin granites (315–314 Ma)—Sources and metal enrichment in Variscan Granites of the Western Erzgebirge (Central European Variscides, Germany). *Minerals* **2019**, *9*, 769. [[CrossRef](#)]
47. Štemprok, M. Intrusion sequences within ore-bearing granitoid plutons. *Geol. J.* **1990**, *25*, 413–417. [[CrossRef](#)]
48. Candela, P.A. A review of shallow, ore-related granites: Textures, volatiles, and ore metals. *J. Petrol.* **1997**, *38*, 1619–1633. [[CrossRef](#)]
49. Štemprok, M. The origin and mineralization of the tin-bearing granites of the Krušnéhory (Erzgebirge) province: A 3-dimensional approach with new data on ore deposit zoning around a granite batholith. *Glob. Tect. Metal.* **2003**, *8*, 215–226.
50. Černý, P.; Ercite, T.S. The classification of granitic pegmatites revisited. *Can. Mineral.* **2005**, *43*, 2005–2026. [[CrossRef](#)]
51. Štemprok, M.; Dolejš, D. Fluid focusing, mass transfer and origin of fracture-controlled greisens in the Western Krušné hory pluton, Central Europe. *Zt. Geol. Wiss.* **2010**, *38*, 207–234.
52. Štemprok, M.; Dolejš, D.; Müller, A.; Seltmann, R. Textural evidence of magma decompression, devolatilization and disequilibrium quenching: An example from the Western Krušné hory/Erzgebirge granite pluton. *Contrib. Mineral. Petrol.* **2008**, *155*, 93–109. [[CrossRef](#)]
53. Wheeler, A. Report NI 43-101: Technical Report on the Mineral Resources and Reserves of Panasqueira Mine. Portugal, 2016; 155p.
54. Neftali da Costa, F. Notas sobre o Jazigo de volfrâmio da Panasqueira. *Bol. Soc. Geológica Port.* **1943**, *3/1-2*, 103–108.
55. Bloor, C.; Wolf, L.C. Geological features of the Panasqueira tin-tungsten ore-occurrence (Portugal). *Bol. Soc. Geológica Port.* **1953**, *11*, 2–75.
56. Thadeu, D. Geologia do Couto Mineiro da Panasqueira. *Commun. Serv. Geol. Port.* **1951**, *32*, 5–64.
57. Thadeu, D. Le gisement stanno-wolframifère de Panasqueira (Portugal). *Chron. Rech. Min.* **1979**, *450*, 35–42.
58. Kelly, W.C.; Reye, R.O. Geologic, fluid inclusion, and stable isotope studies of the tin-tungsten deposits of Panasqueira, Portugal. *Econ. Geol.* **1979**, *74*, 1721–1882. [[CrossRef](#)]
59. Bussink, R.W. Geochemistry of the Panasqueira tungsten-tin deposit, Portugal. *Geol. Ultraiect.* **1984**, *33*, 1–159.
60. Poly, D.A. Efficiency of hydrothermal ore formation and the Panasqueira W-Cu(Ag)-Sn vein deposit. *Nature* **1988**, *333*, 838–841. [[CrossRef](#)]
61. Snee, L.W.; Sutter, F.; Kelly, W.C. Thermochronology of economic mineral deposits: Dating the stages of mineralization at Panasqueira, Portugal by high-precision $^{40}\text{Ar}/^{39}\text{Ar}$ age-spectrum techniques on muscovite. *Econ. Geol.* **1988**, *83*, 335–354. [[CrossRef](#)]
62. Foxford, K.A.; Nicholson, R.; Poly, D.A. Textural evolution of W-Cu-Sn-bearing hydrothermal veins at Minas da Panasqueira, Portugal. *Mineral. Mag.* **1991**, *55*, 435–445. [[CrossRef](#)]
63. Dallmeyer, R.D.; Martínez-Catalán, J.R.; Arenas, R.; Gil-Ibarguchi, J.I.; Gutiérrez-Alonso, G.; Farias, P.; Bastida, F. Diachronous Variscan tectonothermal activity in the NW Iberian Massif; evidence from $^{40}\text{Ar}/^{39}\text{Ar}$ dating of regional fabrics. *Tectonophysics* **1997**, *277*, 307–337. [[CrossRef](#)]
64. Ribeiro, A.; Munhá, J.; Dias, R.; Mateus, A.; Pereira, E.; Ribeiro, M.L.; Fonseca, P.; Araújo, A.; Oliveira, J.T.; Romão, J.; et al. Geodynamic evolution of the SW Europe Variscides. *Tectonics* **2007**, *26*. [[CrossRef](#)]
65. Albuquerque, C.R. Petrochemistry of a series of granitic rocks from northern Portugal. *Geol. Soc. Am. Bull.* **1971**, *82*, 2783–2798. [[CrossRef](#)]
66. Capdevila, R.L.G.; Corretgé, L.G.; Floor, P. Les granitoïdes varisques de la Meseta Ibérique. *Bull. Soc. Geol. Fr.* **1973**, *15*, 209–228. [[CrossRef](#)]
67. Neiva, A.M.R. The geochemistry of biotites from granites of northern Portugal with special reference to their tin content. *Mineral. Mag.* **1976**, *40*, 453–466. [[CrossRef](#)]
68. Neiva, A.M.R. Geochemistry of hybrid granitoid rocks and their biotites from the central northern Portugal and their petrogenesis. *Lithos* **1981**, *14*, 149–163. [[CrossRef](#)]

69. Pinto, M.S. Carboniferous granitoids of Portugal: Some geochemical and geochronological aspects. *Anais Fac. Ciênc. Porto* **1985**, *64*, 15–33.
70. Neiva, A.M.R. Geochemistry of tin-bearing granitic rocks. *Chem. Geol.* **1984**, *43*, 241–256. [[CrossRef](#)]
71. Neiva, A.M.R.; Neiva, J.M.C.; Parry, S.J. Geochemistry of the granitic rocks and their minerals from Serra da Estrela, central Portugal. *Geochim. Cosmochim. Acta* **1987**, *51*, 439–454. [[CrossRef](#)]
72. Pinto, M.S.; Casquet, C.; Ibarrola, E.; Corretgé, L.S.; Ferreira, M.P. Síntese geocronológica dos granitóides do Maciço Hespérico. In *Geologia de los Granitoides y Rocas Asociadas del Macizo Hespérico Libro Homenaje a L. C. Garcia de Figuerola*; Bea, F., Carnicero, E., Gonzalo, J.C., López Plaza, M., Rodríguez, M.D., Eds.; Rueda: Madrid, Spain, 1987; pp. 69–86.
73. Bea, F.; Pereira, M.D.; Corretgé, L.G.; Fershtater, G.B. Differentiation of strongly peraluminous, perphosphorus granites: The Pedrobernardo pluton, central Spain. *Geochim. Cosmochim. Acta* **1994**, *58*, 2609–2627. [[CrossRef](#)]
74. Neiva, A.M.R. Geochemistry of high peraluminous granites and their minerals between Douro and Tamega valleys, northern Portugal. *Chem. Erde* **1998**, *58*, 161–168.
75. Michaud, J.A.S.; Gumiaux, C.; Pichavant, M.; Gloaguen, E.; Marcoux, E. From magmatic to hydrothermal Sn-Li-(Nb-Ta-W) mineralization: The Argemela area (central Portugal). *Ore Geol. Rev.* **2020**, *116*, 103215. [[CrossRef](#)]
76. Valverde-Vaquero, P.; Díez Balda, M.A.; DíezMontes, A.; Dörr, W.; Escuder Viruete, J.; González Clavijo, E.; Maluski, H.; Rodríguez Fernández, L.R.; Rubio, F.; Villar, P. The “Hot Orogen”: Two Separate Variscan Low-Pressure Metamorphic Events in the Central Iberian Zone. In *Mechanics of Variscan Orogeny: A Modern View on Orogenic Research, Géologie de La France*; Faure, M., Lardeaux, J.M., Ledru, P., Peschler, A., Schulmann, K., Eds.; Societé Géologique de France and Bureau de Recherche Géologiques et Minières: Orléans, France, 2007; p. 168.
77. Díez Montes, A.; Martínez Catalán, J.R.; Bellido Mulas, F. Role of the Ollo de Sapo massive felsic volcanism of NW Iberia in the Early Ordovician dynamics of northern Gondwana. *Gondwana Res.* **2010**, *17*, 363–376. [[CrossRef](#)]
78. Gutiérrez-Alonso, G.; Collins, A.S.; Fernández-Suárez, J.; Pastor-Galán, D.; González-Clavijo, E.; Jourdan, F.; Weil, A.B.; Johnston, S.T. Dating of lithospheric buckling: $^{40}\text{Ar}/^{39}\text{Ar}$ ages of syn-oroclinal strike-slip shear zones in northwestern Iberia. *Tectonophysics* **2015**, *643*, 44–54. [[CrossRef](#)]
79. Albuquerque, C.R. Rare earth elements in “younger granites”, northern Portugal. *Lithos* **1978**, *11*, 219–229. [[CrossRef](#)]
80. Dias, G.T. Mineralogia e Petrologia de Granitos Hercínicos Associados a Mineralizações Filonianas de Sn-W (Minho, Portugal). Ph.D. Thesis, Universidade do Minho, Braga, Portugal, 1987; p. 304.
81. Garcia, D. Behaviour of Fe, Mn and Mg during the differentiation of granites and W-Sn bearing hydrothermal activity in the Vila Real area (Northern Portugal). *Bull. Minéral.* **1987**, *110*, 613–622. [[CrossRef](#)]
82. Dias, G.T.; Leterrier, J.; Mendes, A.; Simões, P.P.; Bertrand, J.M. U-Pb zircon and monazite geochronology of post-collisional Hercynian granitoids from the Central Iberian Zone (Northern Portugal). *Lithos* **1998**, *45*, 349–369. [[CrossRef](#)]
83. Neiva, A.M.R.; Gomes, M.E.P. Diferentes tipos de granitos e seus processos petrogenéticos: Granitos hercínicos portugueses. In *Geoquímica e Petrogênese de Rochas Granitóides*; Neiva, A.M.R., Ed.; Mem. Acad. Ciênc.; Academia das Ciências de Lisboa: Lisboa, Portugal, 2001; pp. 53–96.
84. Clauer, N. The post-Variscan tectonic-thermal activity in the southeastern metalliferous province of the French Massif Central revisited with K-Ar ages of illite. *Ore Geol. Rev.* **2020**, *117*, 103300. [[CrossRef](#)]
85. Neiva, J.M.C. Jazigos portugueses de cassiterite e volframite. *Commun. Serv. Geol. Port.* **1944**, *XXV*, 1–251.
86. Thadeu, D. Les gisements stannio-wolframitiques du Portugal. *Ann. Soc. Geól. Bel.* **1973**, *79*, 5–30.
87. Schermerhorn, L.J.G. Framework and evolution of hercynian mineralization in the Iberian Meseta. *Leiden Geologische Mededelingen* **1981**, *52*, 23–56.
88. Derré, C.; Lécolle, M.; Noronha, F.; Roger, G. Minéralisations a Sn-W liées aux granitoides du nord du Portugal: Importance des processus magmatiques et métasomatiques hydrothermaux. *Commun. Serv. Geol. Port.* **1982**, *68*, 191–211.
89. Neiva, A.M.R. On geochemistry and thermodynamic conditions of aplites, pegmatites and hydrothermal quartz veins with cassiterite and wolframite. *Commun. Serv. Geol. Port.* **1982**, *68*, 37–46.
90. Noronha, F. Rochas graníticas do triângulo Gerês-Barroso-Cabreira. Suas relações com mineralizações em Sn e W-Mo. *Pub. Mus. Lab. Min. Geol. Fac. Ciên. Univ. Porto* **1982**, *93*, 1–39.

91. Noronha, F. Estudo Metalogénico da Área Tunstífera da Borralha. Ph.D. Thesis, University Porto, Porto, Portugal, 1983; p. 413.
92. Noronha, F. Caractéristiques physico-chimiques des fluides associés à la genèse du gisement de tungstène de Borralha (Nord du Portugal). *Bull. Mineral.* **1984**, *107*, 273–284. [[CrossRef](#)]
93. Goínhas, J.; Viegas, L. Província metalogenética estanífera e tungsténica ibérica: Considerações sobre as ocorrências de tungsténio em Portugal, sua prospecção e potencialidades. *Estudos, Notas e Trabalhos do Serviço de Fomento Mineiro* **1984**, *XXV*, 147–178.
94. Derré, C.; Roger, G. Filons à étain—Tungstène dans la moitié nord du Portugal. Guides de recherche. *Chron. Rech. Min.* **1984**, *475*, 35–50.
95. Derré, C.; Lécolle, M.; Roger, G.; Carvalho, J. Tectonics, magmatism, hydrothermalism and sets of flat joints locally filled by Sn-W aplite-pegmatite and quartz veins; southeastern border of the Serra da Estrela granitic massif (Beira Baixa, Portugal). *Ore Geol. Rev.* **1986**, *1*, 43–56. [[CrossRef](#)]
96. Derré, C.; Lécolle, R.; Maurel-Palacin, D.; Noronha, F.; Roger, G. Évolution granitique et minéralisations filoniennes à Sn-W dans le Nord du Portugal. *Chron. Rech. Min.* **1987**, *487*, 63–74.
97. Adam, D.; Gagny, C. Contrôle structural et magmatique de la formation de gisements d'étain-tungstène du Trás-os-Montes oriental (Portugal). Guides pour l'exploration minière. *Chron. Rech. Min.* **1989**, *496*, 57–74.
98. Noronha, F.; Vindel, E.; López, J.A.; Dória, A.; Garcia, E.; Boiron, M.-C.; Cathelineau, M. Fluids related to tungsten ore deposits in Northern Portugal and Spanish Central System: A comparative study. *Rev. Soc. Geol. España* **1999**, *12*, 397–403.
99. Tornos, F.; Delgado, A.; Casquet, C.; Galindo, C. 300 Million years of episodic hydrothermal activity: Stable isotope evidence from hydrothermal rocks of the eastern Iberian Central System. *Miner. Deposita* **2000**, *35*, 551–569. [[CrossRef](#)]
100. Ruiz, C.; Fernández-Leyva, C.; Locutura, J. Geochemistry, geochronology and mineralisation potential of the granites in the Central Iberian Zone: The Jálama Batholith. *Geochemistry* **2008**, *68*, 413–429. [[CrossRef](#)]
101. Arthaud, F.; Matte, P. Les décrochements Tardi-Hercyniens du Sud-ouest de l'Europe. Géométrie et essai de reconstitution des conditions de la déformation. *Tectonophysics* **1975**, *25*, 139–171. [[CrossRef](#)]
102. Arthaud, F.; Matte, P. Late Paleozoic strike-slip faulting in Southern Europe and Northern Africa; result of a right lateral shear zone between the Appalachians and the Urals. *Geol. Soc. Am. Bull.* **1977**, *88*, 1305–1320. [[CrossRef](#)]
103. Iglésias, M.; Choukroune, P. Shear zones in the Iberian Arc. *J. Struct. Geol.* **1980**, *2*, 63–68.
104. Iglesias, M.; Ribeiro, A. Zonas de cisaillement dans l'arc ibero-armoricain. *Commun. Serv. Geol. Port.* **1981**, *67*, 85–87.
105. Pereira, E.; Ribeiro, A.; Meireles, C. Cisalhamentos hercínicos e controlo de mineralizações de Sn-W, Au e U na zona centro-Ibérica em Portugal. *Cuad. Lab. Xeol. Laxe Coruña* **1993**, *18*, 89–119.
106. Mateus, A.; Noronha, F. Late-Variscan crustal uplift of the Iberian Terrane as a response to isostatic rebound; implications for the brittle-ductile transition, fluid circulation and metallogenesis. *Mem. Mus. Lab. Mineral. Geol. Univ. Porto* **2001**, *7*, 295–298.
107. Marques, F.O.; Mateus, A.; Tassinari, C.C. The Late-Variscan fault network in central-northern Portugal (NW Iberia): A re-evaluation. *Tectonophysics* **2002**, *359*, 255–270. [[CrossRef](#)]
108. Inverno, C.; Ribeiro, M.L. Fracturação e cortejo filoniano nas Minas da Argemela (Fundão). *Commun. Serv. Geol. Port.* **1980**, *66*, 185–193.
109. Ribeiro, A.; Pereira, E. Controles paleogeográficos, petrológicos e estruturais na génese dos jazigos portugueses de estanho e volfrâmio. *Geonovas* **1982**, *1*, 23–31.
110. Gaspar, L.M.; Inverno, C.M.C. Mineralogy and metasomatic evolution of distal strata-bound scheelite skarns in the Riba de Alva Mine, north-eastern Portugal. *Econ. Geol.* **2000**, *95*, 1259–1275.
111. Noronha, F.; Cathelineau, M.; Boiron, M.-C.; Banks, D.A.; Dória, A.; Ribeiro, M.A.; Nogueira, P.; Guedes, A. A three stage fluid model for Variscan gold metallogenesis in northern Portugal. *J. Geochem. Explor.* **2000**, *71*, 209–224. [[CrossRef](#)]
112. Mateus, A.; Noronha, F. Sistemas mineralizantes epigenéticos na Zona Centro-Ibérica; expressão da estruturação orogénica Meso-a Tardi-Varisca. In *Ciências Geológicas: Ensino e Investigação e sua História*; Coteló Neiva, J.M., Ribeiro, A., Mendes Victor, L., Noronha, F., Ramalho, M., Eds.; Associação Portuguesa de Geólogos and Sociedade Geológica de Portugal, Lisboa: Lisbon, Portugal, 2010; Volume II, pp. 47–61.

113. Lourenço, A. Paleofluidos e Mineralizações Associadas às Fases Tardias da Orogenia Hercínica. Ph.D. Thesis, Universidade do Porto, Porto, Portugal, 2002; p. 326.
114. Póvoa, P. Magnetotelúrica Aplicada à Prospecção Mineira. Master's Thesis, Faculdade de Ciências da Universidade de Lisboa, Lisboa, Portugal, 2011; p. 123.
115. Gonçalves, M.; Mateus, A.; Pinto, F.; Vieira, R. Using multifractal modelling, singularity mapping, and geochemical indexes for targeting buried mineralization: Application to the W-Sn Panasqueira ore-system, Portugal. *J. Geochem. Explor.* **2018**, *189*, 42–53. [[CrossRef](#)]
116. Marignac, C. Analyse structurale de l'environnement du gisement à tungsten-étain de Panasqueira (Beira Baixa, Portugal); Implications génétiques. *C. R. Acad. Sci. Paris Ser.* **1973**, *D277*, 269–272.
117. Foxford, K.A.; Nicholson, R.; Polya, D.A.; Hebbethwalte, R.P.B. Extensional failure and hydraulic valving at Minas da Panasqueira; evidence from vein spatial distributions, displacements and geometries. *J. Struct. Geol.* **2000**, *22*, 1065–1086. [[CrossRef](#)]
118. Jacques, D.; Vieira, R.; Muchez, P.; Sintubin, M. A structural analysis of the Minas da Panasqueira vein network and related fracture generations. In *Geophysical Research Abstracts*; EGU2014-3537; EGU General Assembly: Lund, Sweden, 2014; Volume 16.
119. Jacques, D.; Vieira, R.; Muchez, P.; Sintubin, M.A. Late- to post-orogenic, granite-related fracture reactivation and veining at the Minas da Panasqueira W-Sn-Cu ore deposit (Portugal). *Geotecton. Res.* **2015**, *97*, 53–55. [[CrossRef](#)]
120. Jacques, L.; Pascal, C. Full paleostress tensor reconstruction using quartz veins of Panasqueira Mine, central Portugal; Part I: Paleopressure determination. *J. Struct. Geol.* **2017**, *102*, 58–74. [[CrossRef](#)]
121. Jacques, D.; Vieira, R.; Muchez, P.; Sintubin, M.A. Transpressional folding and associated cross-fold jointing controlling the geometry of post-orogenic vein-type W-Sn mineralization: Examples from Minas da Panasqueira, Portugal. *Miner. Deposita* **2018**, *53*, 171–194. [[CrossRef](#)]
122. Polya, D.A.J. Compositional variation in wolframites from the Barroca Grande mine, Portugal: Evidence for fault-controlled ore formation. *Mineral. Mag* **1988**, *52*, 497–503. [[CrossRef](#)]
123. Lourenço, A.; Noronha, F. Actividade hidrotermal pós-Varisca. Exemplo da mineralização de chumbo em falhas do jazigo da Panasqueira. *Cuad. Lab. Xeol. Laxe* **2000**, *25*, 293–295.
124. Pinto, F. Estudo da distribuição do Estanho na Mina da Panasqueira. Master's Thesis, Faculdade de Ciências da Universidade do Porto, Porto, Portugal, 2014; p. 208.
125. Pinto, F.; Vieira, R.; Noronha, F. Different cassiterite generations at the Panasqueira Deposit (Portugal): Implications for the metal zonation model. In *Mineral Resources in a Sustainable World*; André-Mayer, A.S., Cathelineau, M., Muchez, P., Pirard, E., Sindern, S., Eds.; Proceedings of the Society of Geology Applied to Mineral Deposits (SGA) Biennial Meeting; SGA: Nancy, France, 2015; Volume 2, pp. 827–830.
126. Martins, I. Microanálise Elementar de Sulfuretos, Sulfossais e Carbonatos Constituintes das Associações Polifásicas que Preenchem os Sistemas Filonianos de W(-Sn) Suporte da Mina da Panasqueira (Portugal): Reconhecimento de Marcadores Metalogenéticos. Master's Thesis, Faculdade de Ciências da Universidade de Lisboa, Lisboa, Portugal, 2017; 146p.
127. Oosterm, M.G.; Bussink, R.W.; Vriend, S.P. Litho-geochemical studies of aureoles around the Panasqueira tin-tungsten deposit, Portugal. *Miner. Deposita* **1984**, *19*, 283–288. [[CrossRef](#)]
128. Codeço, M.; Weis, P.; Trumbull, R.; Pinto, F.; Lecumberri-Sanchez, P.; Wilke, F. Chemical and boron isotopic composition of hydrothermal tourmaline from the Panasqueira W-Sn-Cu deposit, Portugal. *Chem. Geol.* **2017**, *468*, 1–16. [[CrossRef](#)]
129. Clark, A.H. Preliminary of the temperatures and confining pressures of granite emplacement and mineralization, Panasqueira, Portugal. *Trans. Inst. Min. Metall.* **1964**, *73*, 813–824.
130. Codeço, M.; Weis, P.; Trumbull, R.; Glodny, J.; Wiedenbeck, M.; Romer, R. Boron isotope muscovite-tourmaline geothermometry indicates fluid cooling during magmatic-hydrothermal W-Sn ore formation. *Econ. Geol.* **2019**, *114*, 153–163. [[CrossRef](#)]
131. Launaya, G.; Sizaret, S.; Guillou-Frottiera, L.; Gloaguena, E.; Melletona, J.; Champallierb, R.; Pichavant, M. Hydrodynamic of ore deposits related to granitic intrusion: Application to the Panasqueira Sn-W-(Cu) deposit (Portugal). In *International Workshop on "Recent Advances in W-Sn and Rare Metal Deposit Metallogenesis"*; GeoResources, University Lorraine: Nancy, France, 2016; Volume Abstract.

132. Launaya, G.; Sizaret, S.; Guillou-Frottiera, L.; Gloaguen, E.; Pinto, F. Deciphering fluid flow at the magmatic-hydrothermal transition: A case study from the world-class Panasqueira W–Sn–(Cu) ore deposit (Portugal). *Earth Planet. Sci. Lett.* **2018**, *499*, 1–12. [[CrossRef](#)]
133. Codeço, M. Constraining the Hydrology at Minas da Panasqueira W–Sn–Cu Deposit, Portugal. Ph.D. Thesis, Faculty of Science of the University of Potsdam, Potsdam, Germany, 2019; p. 232.
134. D’Orey, F.C. Tungsten-tin mineralization and paragenesis in the Panasqueira and Vale de Ermida mining districts, Portugal. *Commun. Serv. Geol. Port.* **1967**, *52*, 117–167.
135. Wimmers, D. Silver minerals of Panasqueira, Portugal: A new occurrence of Te-bearing canfieldite. *Mineral. Mag.* **1985**, *49*, 745–748. [[CrossRef](#)]
136. Carocci, E.; Marignac, C.; Cathelineau, M.; Pinto, F. Tourmaline and W-rutile assemblage as an immediate precursor of wolframite deposition in Panasqueira mine. In *International Workshop on “Recent Advances in W–Sn and Rare Metal Deposit Metallogenesis”*; GeoRessources, University Lorraine: Nancy, France, 2016; Volume Abstract.
137. Carocci, E.; Marignac, C.; Cathelineau, M.; Truche, L.; Lecomte, A.; Pinto, F. Rutile from Panasqueira (Central Portugal): An excellent pathfinder for wolframite deposition. *Minerals* **2019**, *9*, 9. [[CrossRef](#)]
138. Kelly, W.C. The relative timing of metamorphism, granite emplacement and hydrothermal ore deposition in the Panasqueira district (Beira Baixa, Portugal). *Commun. Serv. Geol. Port.* **1977**, *61*, 239–244.
139. Carocci, E.; Marignac, C.; Cathelineau, M.; Pinto, F.; Truche, L. Le stade initial du dépôt de la wolframite dans le gisement à W–Sn–Cu de Panasqueira (Portugal): Caractérisation indirecte des fluides par l’étude des tourmalines précoces. In *Proceedings of the 24th Réunion des Sciences de la Terre, Lille, France, 22–26 October 2018*; p. 439.
140. Zhang, R.; Ramos, V.; Noronha, F.; Pinto, F. U–Pb geochronology of cassiterites from primary Sn mineralizations in Sn–W Variscan Metallogenic Province, Portugal. In *Advances in Understanding Hydrothermal Processes, Life with Ore Deposits on Earth—15th SGA Biennial Meeting*; SGA: Glasgow, Scotland, 2019; Volume 1, pp. 357–360.
141. Turpin, L.; Ramboz, C.; Sheppard, S. Chemical and isotopic evolution of the fluids in the Sn–W deposit, Panasqueira, Portugal. *Terra Cogn. Spec. Issue* **1981**, *42*.
142. Marignac, C. Geologic, fluid inclusions and stable isotope studies of the Panasqueira tungsten-tin deposit, Portugal—A discussion. *Econ. Geol.* **1982**, *77*, 1263–1266. [[CrossRef](#)]
143. Bussink, R.W.; Kreulen, R.; Jong, F.M. Gas analyses, fluid inclusions and stable isotopes of Panasqueira, W–Sn deposit, Portugal. *Bull. Minéral.* **1984**, *107*, 703–713. [[CrossRef](#)]
144. Polya, D.A.J. Chemical Behaviour of Tungsten in Hydrothermal Fluids and Genesis of the Panasqueira W–Cu–Sn Deposit, Portugal. An Experimental, Theoretical and Field Study. Ph.D. Thesis, University of Manchester, Manchester, UK, 1987; p. 243.
145. Campbell, A.; Robinson-Cook, S.; Amindyas, C. Observation of fluid inclusions in wolframite from Panasqueira, Portugal. *Bull. Minéral.* **1988**, *111*, 331–342. [[CrossRef](#)]
146. Polya, D.A.J. Chemistry of the main-stage ore-forming fluids of the Panasqueira W–Cu(Ag)–Sn deposit, Portugal: Implications for models of ore genesis. *Econ. Geol.* **1989**, *84*, 1134–1152. [[CrossRef](#)]
147. Polya, D.A.J. Pressure-dependence of wolframite solubility for hydrothermal vein formation. *Trans. Inst. Min. Metallurg.* **1990**, *99*, 120–124.
148. Noronha, F.; Dória, A.; Dubessy, J.; Charoy, B. Characterization and timing of the different types of fluids present in the barren and ore-veins of the W–Sn deposit of Panasqueira, Central Portugal. *Miner. Deposita* **1992**, *27*, 72–79. [[CrossRef](#)]
149. Lüders, V. Contribution of infrared microscopy to fluid inclusion studies in some opaque minerals (wolframite, stibnite, bournonite): Metallogenic implications. *Econ. Geol.* **1996**, *91*, 1462–1468. [[CrossRef](#)]
150. Polya, D.; Foxford, K.; Stuart, F.; Boyce, A.; Fallick, A. Evolution and paragenetic context of low D hydrothermal fluids from Panasqueira W–Sn deposit, Portugal: New evidence from microthermometric, stable isotope, noble gas and halogen analyses of primary fluid inclusions. *Geochim. Cosmochim. Acta* **2000**, *64*, 3357–3371. [[CrossRef](#)]
151. Burnard, P.G.; Polya, D.A. Importance of mantle derived fluids during granite associated hydrothermal circulation: He and Ar isotopes of ore minerals from Panasqueira. *Geochim. Cosmochim. Acta* **2004**, *68*, 1607–1615. [[CrossRef](#)]

152. Lecumberri-Sanchez, P.; Vieira, R.; Heinrich, C.; Pinto, F.; Wälle, M. Fluid-rock interaction is decisive for the formation of tungsten deposits. *Geology* **2017**, *45*, 579–582. [[CrossRef](#)]
153. Droop, G.A. general equation for estimating Fe³⁺ concentrations in ferromagnesian silicates and oxides from microprobe analyses, using stoichiometric criteria. *Mineral. Mag.* **1987**, *51*, 431–435. [[CrossRef](#)]
154. Ketcham, R.A. Technical Note: Calculation of stoichiometry from EMP data for apatite and other phases with mixing on monovalent anion sites. *Am. Mineral.* **2015**, *100*, 1620–1623. [[CrossRef](#)]
155. Lourenço, A. The Panasqueira granite (Barroca Grande cupola). Study of a granite system associated with tin lodes. *VII Congr. Nac. Geol.* **2006**, 187–190.
156. Henry, D.J.; Guidotti, C.V. Tourmaline as a petrogenetic indicator mineral: An example from the staurolite-grade metapelites of NW Maine. *Am. Mineral.* **1985**, *70*, 1–15.
157. Monier, G.; Robert, J.L. Evolution of the miscibility gap between muscovite and biotite solid solutions with increasing lithium content: An experimental study in the system K₂O-Li₂O-MgO-FeO-Al₂O₃-SiO₂-H₂O-HF at 600 °C, 2 kbar PH₂O: Comparison with natural lithium micas. *Mineral. Mag.* **1986**, *50*, 641–651. [[CrossRef](#)]
158. Hawthorne, F.C.; Henry, D.J. Classification of the minerals of the tourmaline group. *Eur. J. Mineral.* **1999**, *11*, 201–215. [[CrossRef](#)]
159. Henry, D.J.; Dutrow, B.L. Ca substitution in Li-poor aluminous tourmaline. *Can. Mineral.* **1990**, *28*, 111–124.
160. Henry, D.J.; Novák, M.; Hawthorne, F.C.; Ertl, A.; Dutrow, B.L.; Uher, P.; Pezzotta, F. Nomenclature of the tourmaline-super group minerals. *Am. Mineral.* **2011**, *96*, 895–913. [[CrossRef](#)]
161. Bailey, S.W. Classification and structures of micas. In *Micas*; Bailey, S.W., Ed.; Mineralogical Society of America: Washington, DC, USA, 1984; Volume 13, pp. 1–12.
162. Neiva, A.M.R. Geochemistry of white micas from Portuguese tin and tungsten deposits. *Chem. Geol.* **1987**, *63*, 299–317. [[CrossRef](#)]
163. Tischendorf, G.; Gottesmann, B.; Foerster, H.J.; Trumbull, R.B. On Li-bearing micas: Estimating Li from electron microprobe analyses and an improved diagram for graphical representation. *Mineral. Mag.* **1997**, *61*, 809–834. [[CrossRef](#)]
164. Tischendorf, G.; Foerster, H.J.; Gottesmann, B. The correlation between lithium and magnesium in trioctahedral micas: Improved equations for Li₂O estimation from MgO data. *Mineral. Mag.* **1999**, *63*, 57–74. [[CrossRef](#)]
165. Yin, R.; Han, L.; Huang, X.-L.; Li, J.; Li, W.-X.; Chen, L.-L. Textural and chemical variations of micas as indicators for tungsten mineralization: Evidence from highly evolved granites in the Dahutang tungsten deposit, South China. *Am. Mineral.* **2019**, *104*, 949–965. [[CrossRef](#)]
166. Gatta, G.D.; Nestola, F.; Bromiley, G.D.; Loose, A. New insight into crystal chemistry of topaz: A multi-methodological study. *Am. Mineral.* **2006**, *91*, 1839–1846. [[CrossRef](#)]
167. Foster, M.D. Interpretation of the composition and a classification of the chlorites. *USGS Prof. Paper* **1962**, *414*, 33.
168. Bailey, S.W. Chlorites: Structures and crystal chemistry. In *Hydrous Phyllosilicates (Exclusive of Micas)*; Bailey, S.W., Ed.; Mineralogical Society of America: Washington, DC, USA, 1988; Volume 19, pp. 347–403.
169. Wiewiora, A.; Weiss, Z. Crystallochemical classifications of phyllosilicates based on the unified system of projection of chemical composition: II The chlorite group. *Clay Miner.* **1990**, *25*, 83–92. [[CrossRef](#)]
170. Hillier, S.; Velde, B. Octahedral occupancy and the chemical-composition of diagenetic (low-temperature) chlorites. *Clay Miner.* **1991**, *26*, 149–168. [[CrossRef](#)]
171. Vidal, O.; Parra, T.; Vieillard, P. Thermodynamic properties of the Tschermak solid solution in Fe-chlorite: Application to natural examples and possible role of oxidation. *Am. Mineral.* **2005**, *90*, 347–358. [[CrossRef](#)]
172. Clark, J.R.; Williams-Jones, A.E. Rutile as a potential indicator mineral for metamorphosed metallic ore minerals. Deposits. In *Rapport Final de DIVEX, Sous-Projet SC2*; Divex: Montréal, QC, Canada, 2004; 17p.
173. Meinhold, G. Rutile and its applications in earth sciences. *Earth Sci. Rev.* **2010**, *102*, 1–28. [[CrossRef](#)]
174. Möller, P.; Dulski, P.; Szacki, W.; Malow, G.; Riedel, E. Substitution of tin in cassiterite by tantalum, niobium, tungsten, iron and manganese. *Geochim. Cosmoch. Acta* **1988**, *52*, 1497–1503. [[CrossRef](#)]
175. Neiva, A.M.R. Geochemistry of cassiterite and its inclusions and exsolution products from tin and tungsten deposits in Portugal. *Can. Mineral.* **1996**, *34*, 745–768.
176. Neiva, A.M.R. Geochemistry of cassiterite and wolframite from tin and tungsten quartz veins in Portugal. *Ore Geol. Rev.* **2008**, *33*, 221–238. [[CrossRef](#)]

177. Lerouge, C.; Gloaguen, E.; Wille, G.; Bailly, L. Distribution of In and other rare metals in cassiterite and associated minerals in Sn-W ore deposits of the western Variscan Belt. *Eur. J. Mineral.* **2017**, *29*, 739–753. [[CrossRef](#)]
178. Goldmann, S.; Melcher, F.; Gäbler, H.-E.; Dewaele, S.; De Clercq, F.; Muchez, P. Mineralogy and trace element chemistry of ferberite/reinite from tungsten deposits in central Rwanda. *Minerals* **2013**, *3*, 121–144. [[CrossRef](#)]
179. Bowles, J.F. Age dating of individual grains of uraninite in rocks from electron microprobe analyses. *Chem. Geol.* **1990**, *83*, 47–53. [[CrossRef](#)]
180. Bowles, J.F. Age dating from electron microprobe analyses of U, Th, and Pb: Geological advantages and analytical difficulties. *Microsc. Microanal.* **2015**, *21*, 1114–1122. [[CrossRef](#)]
181. Baikie, T.; Ng, G.M.H.; Madhavi, S.; Pramana, S.S.; Blake, K.; Elcombe, M.; White, T.J. The crystal chemistry of the alkaline-earth apatites $A_{10}(PO_4)_6Cu_xO_y(H)_z$ (A = Ca, Sr and Ba). *Dalton Trans.* **2009**, 6722–6726. [[CrossRef](#)] [[PubMed](#)]
182. Mao, M.; Rukhlov, A.S.; Rowins, S.M.; Spence, J.; Coogan, L.A. Apatite Trace Element compositions: A Robust New Tool for Mineral Exploration. *Econ. Geol.* **2016**, *111*, 1187–1222. [[CrossRef](#)]
183. Harlov, D.E. Apatite: A fingerprint for metasomatic processes. *Elements* **2015**, *11*, 171–176. [[CrossRef](#)]
184. Bruand, E.; Fowler, M.; Storey, C.; Darling, J. Apatite trace element and isotope applications to petrogenesis and provenance. *Am. Mineral.* **2017**, *102*, 75–84. [[CrossRef](#)]
185. Antonakos, A.; Liarokapis, L.; Kyriacou, A.; Leventouri, T. Raman and IR studies of the effect of Fe substitution in hydroxyapatites and deuterated hydroxyapatite. *Am. Mineral.* **2017**, *102*, 85–91. [[CrossRef](#)]
186. Cox, S.J. Coupling between deformation, fluid pressures, and fluid flow in ore-producing hydrothermal systems at depth in the crust. In *Economic Geology*; Hedenquist, J.W., Thompson, J.F.H., Goldfarb, R.J., Richards, J.R., Eds.; Society of Economic Geologists, Inc.: Littleton, CO, USA, 2005; Volume 100th Anniversary, pp. 39–75.
187. London, D.; Morgan, G.B.; Wolf, M.B. Boron in granitic rocks and their contact aureoles. In *Boron, Mineralogy, Petrology and Geochemistry in the Earth's Crust*; Grew, E., Anovitz, L., Eds.; Mineralogical Society of America: Washington, DC, USA, 1996; Volume 33, pp. 299–330.
188. Heinrich, C.A. The chemistry of hydrothermal tin(-tungsten) ore deposition. *Econ. Geol.* **1990**, *85*, 457–481. [[CrossRef](#)]
189. Linnen, R.L.; Cuney, M. Granite-related rare-element deposits and experimental constraints on Ta-Nb-W-Sn-Zr-Hf mineralization. In *Rare Element Geochemistry and Mineral Deposits*; Linnen, R.L., Samson, I.M., Eds.; Geological Association of Canada Short Course Notes; Geological Association of Canada: St. John's, NL, Canada, 2005; Volume 17, pp. 45–68.
190. Teiber, H.; Marks, M.A.W.; Wenzel, T.; Siebel, W.; Altherr, R.; Markl, G. The distribution of halogens (F, Cl, Br) in granitoid rocks. *Chem. Geol.* **2014**, *374*, 92–109. [[CrossRef](#)]
191. Zack, T.; Moraes, R.; Kronz, A. Temperature dependence of Zr in rutile: Empirical calibration of a rutile thermometer. *Contrib. Mineral. Petrol.* **2004**, *148*, 471–488. [[CrossRef](#)]
192. Watson, E.B.; Wark, D.A.; Thomas, J.B. Crystallization thermometers for zircon and rutile. *Contrib. Mineral. Petrol.* **2006**, *151*, 413–433. [[CrossRef](#)]
193. Ferry, J.M.; Watson, E.B. New thermodynamic models and revised calibrations for the Ti-in-zircon and Zr-in-rutile thermometers. *Contrib. Mineral. Petrol.* **2007**, *154*, 429–437. [[CrossRef](#)]
194. Van Hinsberg, V.J.; Schumacher, J.C. Intersector element partitioning in tourmaline: A potentially powerful single crystal thermometer. *Contrib. Mineral. Petrol.* **2007**, *153*, 289–301. [[CrossRef](#)]
195. Barton, M.D. The thermodynamic properties of topaz solid solutions and some petrologic applications. *Am. Mineral.* **1982**, *67*, 956–974.
196. Halter, W.E.; Williams-Jones, A. Application of topaz-muscovite F-OH exchange as a geothermometer. *Econ. Geol.* **1999**, *94*, 1249–1258. [[CrossRef](#)]
197. Walshe, J.L. A six-component chlorite solid solution model and the conditions of chlorite formation in hydrothermal and geothermal systems. *Econ. Geol.* **1986**, *81*, 681–703. [[CrossRef](#)]
198. Cathelineau, M. Cation site occupancy in chlorites and illites as a function of temperature. *Clay Miner.* **1988**, *23*, 471–485. [[CrossRef](#)]
199. De Caritat, P.; Hutcheon, I.; Walshe, J.L. Chlorite geothermometry: A review. *Clays Clay Miner.* **1993**, *41*, 219–239. [[CrossRef](#)]

200. Vidal, O.; Parra, T.; Trotet, F. A thermodynamic model for Fe-Mg aluminous chlorite using data from phase equilibrium experiments and natural pelitic assemblages in the 100 to 600 °C, 1 to 25 kb range. *Am. J. Sci.* **2001**, *301*, 557–592. [[CrossRef](#)]
201. Inoue, A.; Meunier, A.; Patrier-Mas, P.; Rigault, C.; Beaufort, D.; Vieillard, P. Application of chemical geothermometry to low-temperature trioctahedral chlorites. *Clays Clay Miner.* **2009**, *57*, 371–382. [[CrossRef](#)]
202. Bourdelle, F.; Parra, T.; Chopin, C.; Beyssac, O. A new chlorite geothermometer for diagenetic to low-grade metamorphic conditions. *Contrib. Mineral. Petrol.* **2013**, *165*, 723–735. [[CrossRef](#)]
203. Lanari, P.; Wagner, T.; Vidal, O. A thermodynamic model for di-trioctahedral chlorite from experimental and natural data in the system MgO–FeO–Al₂O₃–SiO₂–H₂O: Applications to P–T sections and geothermometry. *Contrib. Mineral. Petrol.* **2014**, *167*, 968. [[CrossRef](#)]
204. Martins, I.; Mateus, A.; Figueiras, J.; Rodrigues, P.; Pinto, F. Thermal evolution of the W-Sn(-Cu) Panasqueira ore system (Portugal): Insights from pyrite-pyrrhotite and arsenopyrite geothermometers. *Comunicações Geológicas* **2020**, in press.



© 2020 by the authors. Licensee MDPI, Basel, Switzerland. This article is an open access article distributed under the terms and conditions of the Creative Commons Attribution (CC BY) license (<http://creativecommons.org/licenses/by/4.0/>).